Research paper

Material Extrusion Additive Manufacturing of Poly(Lactic Acid): Influence of infill orientation angle

Wilco M.H. Verbeeten [*], Miriam Lorenzo-Bañuelos

Structural Integrity Research Group, Universidad de Burgos, Avenida Cantabria s/n, E-09006, Burgos, Spain

A B S T R A C T

The effect that the infill orientation angle has on the strain-rate dependence of the yield stress for material extrusion additive manufactured (ME-AM) PolyLactic Acid (PLA) material was investigated. Symmetric angle-ply stacking sequences were used to produce ME-AM tensile test samples. Measured yield stresses were compensated for the voided structure, typical of ME-AM components. Furthermore, molecular orientation and stretch was macroscopically assessed by a thermal shrinkage procedure. Additionally, hot-press compression molded (*CM*) samples were manufactured and mechanically characterized in uniaxial tensile and compression in order to determine the material's isotropic bulk properties. Initial model parameters for the Ree–Eyring modification of the Eyring flow rule were determined using *CM* data. According to SEM fractography, all samples showed microscopically brittle fracture behavior. Notwithstanding, contrary to *CM* samples, ME-AM specimens showed macroscopically ductile stress–strain behavior and a transition from a regime with only a primary α-deformation process, at low strain rates, to a regime with 2 deformation processes ($\alpha + \beta$), at high strain rates. These effects are an influence of the processing step and are attributed to the molecular orientation and stretch of the polymer chains, provoking anisotropic mechanical properties. As a consequence, a deformation-induced change of the Eyring rate constants is needed to adequately describe the strain-rate dependence of the ME-AM yield stress behavior, leaving the initial activation volumes unchanged. Taking this deformation-dependence of the rate constants into account, yield stresses as a function of infill orientation angle can be appropriately predicted.

1. Introduction

Material Extrusion Additive Manufacturing (ME-AM) [1], also known as Fused Deposition Modeling (FDM®), Fused Filament Fabrication (FFF), Fused Layer Modeling (FLM), or 3D printing, is one of the most widely used Additive Manufacturing (AM) techniques for polymer materials. It is attracting a lot of attention from both industry as well as research groups, as it can be effectively used for end-user manufacturing. Its popularity is due to a combination of low investment costs, availability of a wide range of materials, and ease for manufacturing [2,3]. Furthermore, components with good and near-bulk mechanical properties can be obtained, if proper processing parameters are chosen [4–7].

The equipment for ME-AM technology consists of a pinch roller mechanism that pushes a thermoplastic polymer filament through a heated liquefier. The molten polymer is consequently extruded through a nozzle, and deposited in a controlled manner onto a (heated) build platform or an already deposited and solidified layer. In such a way, complex 3D products can be constructed layer by layer. During the

ME-AM process, material elements experience time–temperature (initial fast cooling combined with successive heating cycles) and time–strain profiles [8–14], which are significantly different from more conventional methods, *e.g.* injection or compression molding techniques. Both profiles are influenced by the chosen printing process parameters [15,16], and provoke specific macroscopic deformation behavior as measured in macroscopic characterization tests (*e.g.* tensile, compression, shear, torsion, bending, creep, fatigue, impact). The time–temperature profile affects bonding between the extruded filament and the already cooled adjacent strands though the wetting and molecular diffusion process driven by reptation [11,12,17]. Shear effects in the nozzle and the curvature between nozzle and deposited filament can lead to orientation and stretch of the polymer chain [11,13]. For amorphous polymers, frozen-in flow-induced molecular orientation can emerge [16,18]. While for semi-crystalline polymers, it can cause oriented crystalline microstructures (*i.e.* shish-kebab morphology) due to flow-induced crystallization [19]. For both type of polymers, this produces local anisotropy. Hence, the resulting end-product is a locally

anisotropic laminar composite structure consisting of stacked layers of partially bonded filaments with interstitial voids [9,16].

One of the printing parameters that has a significant influence on the mechanical properties is the infill orientation angle [20–25]. It can even be used to control and fine-tune mechanical properties in the direction of the build platform (*i.e.* the XY-plane), similar to composite structures. However, in order to accomplish that, a good understanding of its influence on the mechanical properties is necessary.

Several research groups have investigated the effect of the infill orientation angle on mechanical properties. Different studies have opted for various strategies to achieve different angles between the strand orientation and the applied load.

Unidirectional printed Acrylonitrile–Butadiene–Styrene (ABS) specimens were used by Rodríguez et al. [21], *i.e.* samples where the infill strand deposition angle of all layers is in the same direction. They showed that the yield strength as a function of strand orientation could be satisfactorily predicted by the Azzi and Tsai failure theory [26] for composite laminates. Lanzotti et al. [22] also used unidirectional samples. However, the layer thickness and number of perimeters used in their study on PolyLactic Acid (PLA) material were not constant for the different infill angles. Song et al. [5] and Afrose et al. [27] also opted for unidirectional samples, both using a PLA material. Song et al. conducted tension and compression tests at two different strain rates and 3 orientations, as well as fracture experiments and compared the results with injection molded specimen [5]. While Afrose et al. investigated the fatigue behavior at 3 orientations [27].

Since ME-AM has similarities with laminar composite structures, often theory, nomenclature, and notations for lamina stacking sequence from that research area are adopted. One of the most commonly used infill orientation angle configurations for 3D printing is a so-called orthogonal angle-ply laminate configuration [28]. Such a configuration has a repetition of one layer at a certain infill angle and the next at an angle perpendicular to that. A standard default configuration is indicated by the notation [45°/−45°], and consists of one layer at a 45° angle and the next at a −45° angle, leading to a criss-cross raster laminate structure. Another often used orthogonal angle-ply configuration is [0°/90°]. Among others, Tymrak et al. [29] used these two configurations to investigate ABS and PLA materials, Ning et al. [30] for chopped carbon fiber-reinforced ABS, and Papon & Haque [31] for short carbon fiber-reinforced PLA. Several other research groups compared orthogonal angle-ply specimen with unidirectional samples, *e.g.*, to investigate ABS material [32], fatigue properties of PLA material [6], or mechanical strength and fatigue properties for Ultem (*i.e.* PolyEtherImide (PEI)) and PolyEtherKetoneKetone (PEKK) materials [33].

A more complete set of orthogonal angle-ply specimen, *i.e.* [0°/90°], [15°/−75°], [30°/−60°], and [45°/−45°], was adopted by Li et al. [20] and Dawoud et al. [23] for ABS material, and by Ahmed & Susmel [24] to investigate PLA material. Messimer et al. [34] executed a very complete study for eleven polymer materials, using 7 orthogonal angle-ply sample sets ranging from 0° to 90° in 15° increments for each material. Unfortunately, only dimensional error was measured, but no mechanical strength properties.

Another sort of orientation configuration often used in laminar composite structures, is the (anti)symmetric angle-ply configuration. These specimen consist of an odd or even number of identical orthotropic layers oriented alternately at angles θ and $-\theta$ [28,35], indicated as [$\theta/-\theta$]. Kain et al. [25] used 7 different angle-ply samples from 0° to 90° at 15° intervals for their research on PLA/wood specimen. Note that this is a different set of samples than the *orthogonal* angle-ply configuration applied by *e.g.* Messimer et al. [34].

Occasionally, *pseudo-isotropic* samples are used for investigation purposes [36], *e.g.* by using a [0°/90°/45°/−45°] infill orientation stacking sequence. In laminar composite terms, such a configuration is also indicated as *quasi-isotropic* laminates [28]. Mechanical properties in the XY-plane are practically independent of the load direction for such a configuration. Although macroscopically isotropic in the XY-plane, inherently these ME-AM samples still have *local* anisotropy [18].

Save the study by Song et al. [5], the authors have not encountered scientific articles that investigated the effect of infill orientation angle on mechanical properties and also took strain-rate dependence into account. However, Song et al. [5] measured 3 unidirectional sample configurations at only 2 different strain rates, which resulted in a rather narrow strain-rate range of a single decade.

Yet, strain-rate sensitivity of the yield stress is a manifestation of a polymer material's viscoelastic behavior [37–40]. And viscoelasticity is a crucial characteristic to predict a component's ultimate failure behavior. This not only holds for short-term experiments (*e.g.* uniaxial tensile or compression tests), but also for long-term failure behavior, as manifested in creep and fatigue measurements [41–43].

The present study is focused on the effect that the infill orientation angle has on the strain-rate dependence of the yield stress for a PolyLactic Acid (PLA) material. Only samples oriented in the printer's XY-plane are considered. Although the objective is somewhat similar to a previous study [7], the present research includes several novelties:

(i) Hot-press compression molded (*CM*) samples are manufactured and mechanically characterized in both uniaxial tensile *and* compression tests, in order to determine the PLA material's *isotropic* bulk reference properties. By measuring in more than one loading geometry (*i.e.* uniaxial tensile and compression), a more complete and precise set of parameters for an Eyring-type flow rule [37,44] can be established [45]. For instance, thermorheologically complex behavior can be more easily detected in uniaxial compression tests [46]. Besides, an initial reference set for the Eyring-type flow rule sheds light on the polymer's viscoelastic behavior [39], and how the ME-AM process influences that viscoelastic behavior.

(ii) Samples fabricated by the ME-AM technique are measured at more strain rates in a broad strain-rate spectrum ($\dot{\varepsilon} = 10^{-5} - 10^{-1} \text{ s}^{-1}$). The advantage of measuring more strain rates is that transitions due to the appearance of an additional molecular relaxation process become more apparent [45,47].

(iii) An ample range of 7 different symmetric angle-ply stacking sequences (from 0° to 90° at 15° intervals) is used to produce ME-AM sample sets, similar to what was used by Kain et al. [25] in their study for wood-filled PLA. This is significantly more compared to the two unidirectional sets (longitudinal [0°] and transverse [90°]) that were used in the previous study [7]. Hence, infill orientation effects become more visible.

(iv) Both *CM* and ME-AM sample sets are compared to each other and, additionally, to an ME-AM *quasi-isotropic* sample set with a [0°/90°/45°/−45°] stacking sequence. For all these sets, the Eyring-type flow rule is evaluated to predict yield stress performance.

As far as the authors know, the combination of these four aspects has not been published before by other research groups.

The results of the present study can aid to better understand the influence of the infill orientation angle of deposited polymer strands on mechanical properties. Furthermore, it can help to further develop predictive numerical tools that can quantitatively predict the performance of material extrusion additively manufactured components. Especially since Eyring-type flow rules can be satisfactorily incorporated in accurate constitutive models for polymer materials [48–51].

2. Materials and methods

2.1. Material

The material used for the present study is a commercially available natural transparent Polylactide (PLA) filament (Orbi-Tech, Leichlingen, Germany) with a nominal diameter of 1.75 mm and a specific gravity of 1.25 g cm^{-3}. Recommended nozzle and bed temperatures range from 195 °C to 240 °C and from 40 °C to 60 °C, respectively. All samples were fabricated from a single spool, and the filament was used as-received.
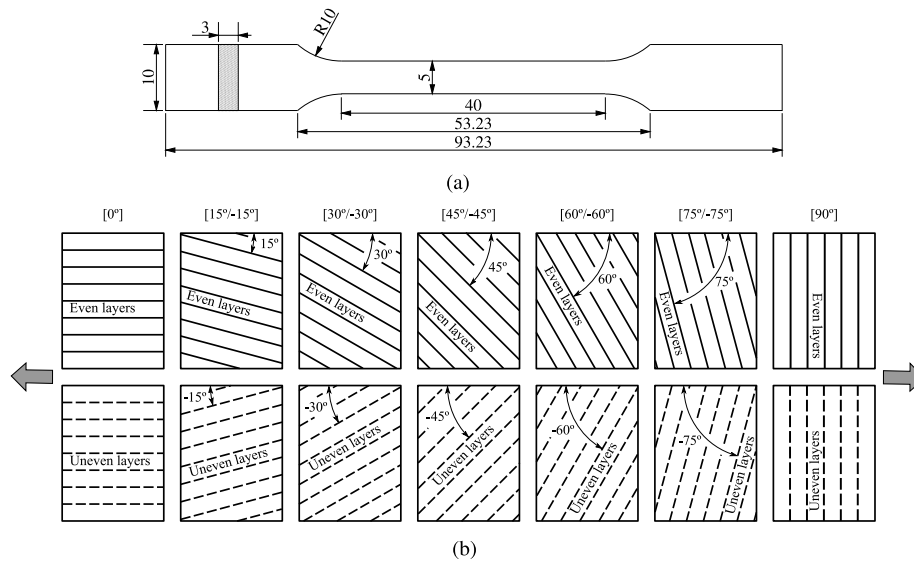
Fig. 1. *(a)* Tensile test specimen dimensions in mm. *(b)* Schematic of the angle-ply infill orientation stacking sequence. Gray arrows indicate force direction in uniaxial tensile tests.

Table 1
Processing parameters used to manufacture ME-AM tensile samples.

Processing parameter	Value
Nozzle diameter [mm]	0.40
Extrusion width [mm]	0.30
Extrusion multiplier	1.00
Layer height [mm]	0.20
Number of perimeters	2
Fill percentage	100%
Outline overlap	80%
Extrusion temperature [°C]	205
Bed temperature [°C]	50
Printing speed v_p [mm s^{-1}]	35

Table 2
Lamina stacking sequence to manufacture different sets of ME-AM tensile samples.

Set nomenclature	Infill orientation stacking sequence
PLAo00	[0°]
PLAo15	[15°/−15°]
PLAo30	[30°/−30°]
PLAo45	[45°/−45°]
PLAo60	[60°/−60°]
PLAo75	[75°/−75°]
PLAo90	[90°]
PLAoISO	[0°/90°/45°/−45°]

2.2. Material processing

Tensile samples were manufactured on an open-source Prusa P3steel 3D printer (Orballo Printing C.B., Vigo, Spain) using a 0.4 mm nozzle size. Sample dimensions are given in Fig. 1(a). This tensile test specimen is based on Specimen type 1BA according to the ISO 527-2 norm, but adapted to avoid fracture in the fillet [7]. The dimensions were chosen in such a way that they could also be machined from compression molded square plates.

An STL file of the tensile sample was imported in the Simplify3D slicing software (version 3.1.1). The printing parameters used to produce all ME-AM sample sets are given in Table 1. Note that an outline overlap of 80% was used to produce the test specimens. This affects only one of the perimeter outlines, and was chosen in order to avoid large gaps in the curved parts of the samples. It could, however, introduce additional residual stresses in the samples' edges.

Sets of ME-AM samples with different infill orientation angles were produced, using a symmetric angle-ply stacking sequence. In total, 7 sets of angle-ply samples from 0° to 90° at 15° intervals were printed. Additionally, a set of *quasi-isotropic* samples with a [0°/90°/45°/−45°] stacking sequence was manufactured. In Table 2, the stacking sequence of the different sets are indicated and a schematic is given in Fig. 1(b). The reference line to indicate the infill angle is the main axis of the tensile specimen, and coincides with the sample loading direction. An image of the printed and tensile tested (at $\dot{\varepsilon} = 10^{-3}$ s^{-1}) samples for different configurations is shown in Fig. 2. After given the right processing parameters and stacking sequence to the test specimen, the sample was copied 18 times and distributed evenly on the printer's XY plane. Thus, a total of 8 sets were printed, each set consisted of 18 samples and was manufactured with a single G-code file.

2.3. Hot-press compression molding

In order to obtain test specimen with isotropic bulk properties, *i.e.* specimen with a minimum of molecular orientation, samples were extracted from hot-press compression molded (*CM*) plates. During the initial phase of compression molding, the material was heated and able to relax its possible residual orientation, leading to isotropic samples at the end of the fabrication cycle. This contrary to injection molding, where molecular orientation can be introduced during processing [52–54]. The hot-press compression molding technique was used to produce both isotropic tensile and compression test samples.

For the tensile test specimen, square plates with dimensions of 100×100 × 3 mm³ were compression molded in a hot press. Approximately 45 gr of chopped filament strands were preheated in the mold at 210 °C for 15 min. Subsequently, the material was compressed during 5 min in successive steps of 5 bar by increasing the pressure from 5 bar to 20 bar and allowing degassing by releasing pressure between steps. Next, cooling to room temperature was established by placing the mold into a cold press at a moderate pressure of 10 bar during another 5 min. From these square plates, tensile test samples were cut with a LASER PC60/40 laser cutting machine (PerezCamps, Viladecans, Spain) at 48 W power and 1000 mm min^{-1} speed with the dimensions as given in Fig. 1(a). Sample edges were straight and smooth and showed no excessive melting or any burn marks after visual inspection. However, thermal effects due to laser cutting cannot completely be excluded.

For the compression test specimen, a square plate with dimensions of 100×100×8 mm³ was produced using the same compression molding procedure. Here, approximately 120 gr of chopped filament strands were used. From the square plate, cylindrical compression test samples
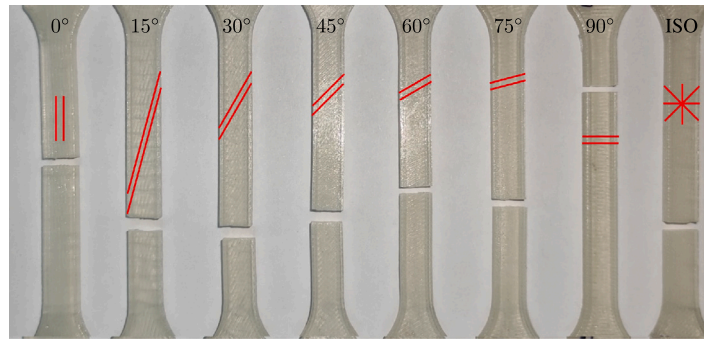
Fig. 2. Image of tensile tested ME-AM samples with different stacking sequences.

were carefully turned on a CNC lathe in order to maintain a high level of parallelism and perpendicularity. The test specimens had a height and diameter of 6 mm.

2.4. Mechanical characterization

Uniaxial tensile tests were performed on a MTS Criterion C43.104 universal test system with a 10 kN load cell. All experiments were measured at room temperature (23 °C). Constant nominal strain rates were applied in the range from 10^{-5} s^{-1} to 10^{-1} s^{-1}. Three samples were used for every single strain rate, obtaining good repeatability and low standard deviations (see also Table A.2). As is common for polymers, the first maximum stress value in the engineering stress–strain curves is considered as the polymer's yield stress. Conversion from engineering to true yield stresses was accomplished by assuming that the material volume remains constant during uniaxial tensile testing [47,55]. This is standard in polymer engineering, and according to Govaert et al. [56] it introduces a small error of approximately 2% compared to a compressible approach.

For uniaxial compression tests, the cylindrical samples were compressed between two parallel flat steel platens, mounted in the same MTS Criterion C43.104 universal test system. To reduce friction in order to avoid bulging or buckling of the samples, a thin PTFE skived film tape (3M 5480) was attached to the sample ends and the surface between steel platens and tape was lubricated with a PTFE spray. Homogeneous deformation during the complete compression test range was observed, indicating that friction was sufficiently reduced. Constant nominal strain rates ranging from $3 \cdot 10^{-4}$ s^{-1} to 10^{-1} s^{-1} were applied at room temperature. Three test samples were used for every single strain rate. Since homogeneous deformation was obtained during testing, even at large strains, true stress–strain curves can be directly determined from the uniaxial compression tests under the assumption of incompressibility and applying a correction for the machine set-up stiffness.

2.5. Apparent density

Due to the fact that ME-AM parts generally have interstitial voids, its mechanical properties are affected by this voided structure. To compensate for this and provide a more fair comparison of the material behavior, the apparent densities of the resulting ME-AM samples were determined before performing mechanical characterization. Both mass and external volume were measured for every single sample to calculate the apparent density:

$$\rho_{app} = \frac{m_{sample}}{V_{sample}} \ . \tag{1}$$

Furthermore, an approximation of the porosity of the samples (in percentage) was determined by using the material density as given by the filament provider, *i.e.* $\rho_{PLA} = 1.25$ g cm^{-3}:

$$Porosity = \frac{\rho_{PLA} - \rho_{app}}{\rho_{PLA}} \cdot 100\% \ . \tag{2}$$

Hence, by multiplying measured yield stresses σ_y with the material's reference density and divide it by the apparent density, *void corrected* yield stresses $\sigma_{y,vc}$ can be calculated:

$$\sigma_{y,vc} = \sigma_y \cdot \frac{\rho_{PLA}}{\rho_{app}} \ . \tag{3}$$

This calculation is done for every single sample separately.

2.6. Thermal shrinkage

For assessment of molecular orientation and stretch, a qualitative macroscopic measurement procedure was applied that is based on thermal shrinkage [16]. It consisted of measuring the ME-AM sample dimensions at room temperature. Next, the ME-AM samples were heated in an oven at 100 °C for six hours. As determined using DSC measurements on the same material by Verbeeten et al. [7], this is a temperature well above the glass transition temperature ($T_g = 66$ °C) and below the cold crystallization temperature ($T_c = 122$ °C). At this temperature and during this time, the molecular chains are able to relax. Then, the samples were cooled back to room temperature and their dimensions were measured again. Expansion(+)/contraction(−) can be determined from dimensional differences. Three samples for each printed set were used for this thermal shrinkage procedure. In order to determine if and to what extent cold crystallization affected the dimensional shrinkage, Verbeeten et al. [7] performed DSC measurements on samples, which were elaborated at various printing velocities and two different raster angles. Both recently printed samples and samples that had undergone thermal shrinkage were measured. Crystallinities for the untreated ME-AM samples were below 2%. All thermally treated samples had similar crystallinities around 38%, but significantly different dimensional changes. Furthermore, all samples demonstrated dimensional contraction in the strand directions and expansion in the direction perpendicular to the strand deposition. Hence, it was concluded from the combination of thermal shrinkage and DSC measurements, that cold crystallization had a similar shrinkage effect on all samples, and that the *variations* in dimensional changes were indicative to the degree of molecular chain orientation and stretch due to the processing phase [7].

2.7. Scanning Electron Microscope fractography

Following uniaxial tensile tests, the fracture surface of several samples were observed using a JEOL JSM-6460LV scanning electron microscope (SEM). The samples were prepared by sputter-coating with an Au-coating. Samples were observed under vacuum and an accelerating voltage of 20.00 kV.

Table 3

Definitions of the equivalent (plastic) shear rate, $\dot{\bar{\gamma}}$, shear stress, $\bar{\tau}$, and hydrostatic pressure, p, expressed in components of the deformation and stress tensor. Explicit expressions are given for tension, compression, and shear.

Definition	Tension	Compression	Shear
$\dot{\bar{\gamma}} = \sqrt{2\left(\dot{\varepsilon}_{11}^2 + \dot{\varepsilon}_{22}^2 + \dot{\varepsilon}_{33}^2 + 2\dot{\varepsilon}_{12}^2 + 2\dot{\varepsilon}_{13}^2 + 2\dot{\varepsilon}_{23}^2\right)}$	$\sqrt{3}\dot{\varepsilon}$	$\sqrt{3}\|\dot{\varepsilon}\|$	$\dot{\gamma}$
$\bar{\tau} = \sqrt{\frac{1}{6}\left[(\sigma_{11}-\sigma_{22})^2 + (\sigma_{22}-\sigma_{33})^2 + (\sigma_{33}-\sigma_{11})^2\right] + \sigma_{12}^2 + \sigma_{13}^2 + \sigma_{23}^2}$	$\frac{\sigma}{\sqrt{3}}$	$\frac{\|\sigma\|}{\sqrt{3}}$	τ
$p = -\frac{1}{3}\left(\sigma_{11} + \sigma_{22} + \sigma_{33}\right)$	$-\frac{\sigma}{3}$	$+\frac{\|\sigma\|}{3}$	0

3. Modeling

It has been shown frequently over the years [39,42,55,57–60], that the deformation kinetics of polymer materials can be adequately described by a linear dependence of the yield stress on the logarithm of strain rate, on temperature, and on pressure. For polymers with a thermorheologically simple response [39], an Eyring-type pressure-modified rate equation [58] can quantitatively capture the yield stress behavior:

$$\dot{\bar{\gamma}}(T, \bar{\tau}, p) = \dot{\gamma}_0 \exp\left(-\frac{\Delta U}{RT}\right) \exp\left(-\frac{\mu p V^*}{kT}\right) \sinh\left(\frac{\bar{\tau} V^*}{kT}\right) . \tag{4}$$

Here, $\dot{\bar{\gamma}}$ is the equivalent plastic shear rate, T the absolute temperature in K, $\bar{\tau}$ the equivalent shear stress, p the hydrostatic pressure, $\dot{\gamma}_0$ a rate constant, ΔU the activation energy, R the universal gas constant (8.314472 J mol^{-1} K^{-1}), μ a pressure dependence parameter, V^* the activation volume, and k is the Boltzmann's constant (1.38054 · 10^{-23} J K^{-1}).

The prefix $\dot{\gamma}_0$ is a rate constant that reduces with diminished molecular mobility [46]. It depends on the thermodynamic state of the material and is related to the density increase due to physical aging [51], which restricts molecular mobility. The first exponential term, which includes the activation energy ΔU, covers the material's temperature dependence. The last term, a hyperbolic sine function that includes the activation volume V^*, determines the stress and strain-rate dependency of the material [38,58]. The second exponential term, which includes the pressure dependence parameter μ, captures the effect of hydrostatic pressure [58,60], *i.e.* negative for tensile tests and positive for compression tests.

Definitions for the equivalent plastic shear rate $\dot{\bar{\gamma}}$ (based on the second invariant of the rate of strain tensor), equivalent shear stress $\bar{\tau}$ (based on the second invariant of the deviatoric stress tensor), and hydrostatic pressure p are given in Table 3. Expressions for uniaxial tension, uniaxial compression, and pure shear are also given in Table 3, and show that the equivalent stress and shear rate are equal to the values measured in a pure shear test.

If written in terms of the equivalent shear stress as a function of equivalent shear rate, the equation reads:

$$\bar{\tau}(T, \dot{\bar{\gamma}}, p) = \frac{kT}{V^*} \sinh^{-1}\left[\frac{\dot{\bar{\gamma}}}{\dot{\gamma}_0} \exp\left(\frac{\Delta U}{RT}\right) \exp\left(\frac{\mu p V^*}{kT}\right)\right] . \tag{5}$$

Note that true stress values are referred to in these equations.

In addition, many polymers exhibit two (or even more) molecular relaxation processes, termed as thermorheologically complex behavior. It was illustrated previously [42,46], that PolyLactic Acid also manifests two molecular deformation processes ($\alpha + \beta$). The effect of more than one molecular relaxation process can become visible by a change in the slope in the yield stress vs. logarithmic strain-rate plots [55]. Another way for detecting multiple relaxation processes is a possible difference between the slope of the upper-yield vs. logarithmic strain-rate and the slope of the lower-yield vs. logarithmic strain-rate in uniaxial compression tests [42,46]. In these cases, the yield behavior can be well described by the Ree–Eyring modification [37] of the Eyring-type flow rule, where it is assumed that different molecular processes act independently and in parallel:

$$\bar{\tau}(T, \dot{\bar{\gamma}}, p) = \sum_{x=\alpha}^{\beta} \frac{kT}{V_x^*} \sinh^{-1}\left[\frac{\dot{\bar{\gamma}}}{\dot{\gamma}_{0,x}} \exp\left(\frac{\Delta U_x}{RT}\right) \exp\left(\frac{\mu_x p_x V_x^*}{kT}\right)\right] . \tag{6}$$

Here, x relates to the indication of the parameters related to each relaxation process, α and β, with decreasing temperature. Commonly, the molecular processes are related to a main-chain segmental motion (the primary glass- or α-transition) and a partial side-chain mobility (a secondary or β-transition) [46].

By making use of the expressions in Table 3, the pressure-dependent Ree–Eyring flow rule (Eq. (6)) can be simplified to describe the true yield stresses for both tensile as well as compression tests. This results for the uniaxial tensile tests in:

$$\sigma_y^T = \sum_{x=\alpha}^{\beta} \frac{3}{\sqrt{3}+\mu_x} \frac{kT}{V_x^*} \sinh^{-1}\left[\frac{\sqrt{3}\dot{\varepsilon}}{\dot{\gamma}_{0,x}} \exp\left(\frac{\Delta U_x}{RT}\right)\right] , \tag{7}$$

while for the uniaxial compression tests in:

$$|\sigma_y^C| = \sum_{x=\alpha}^{\beta} \frac{3}{\sqrt{3}-\mu_x} \frac{kT}{V_x^*} \sinh^{-1}\left[\frac{\sqrt{3}|\dot{\varepsilon}|}{\dot{\gamma}_{0,x}} \exp\left(\frac{\Delta U_x}{RT}\right)\right] . \tag{8}$$

Note that the only difference resides in the opposite sign for the hydrostatic pressure parameter μ_x. This not only accounts for a difference between the yield stress under different loading geometries (*i.e.* uniaxial tensile, simple shear, uniaxial compression), but also for a distinct strain-rate dependence. This last characteristic can be used to determine the influence of the hydrostatic pressure and its corresponding parameter μ [45,47,56,60].

4. Results and discussion

The PLA material used in the present study is the same as previously used [7]. From that previous study, it was concluded that the composition probably consists of a Poly(L-Lactic Acid) polymer (PLLA) with a D content of approximately 4%. The measured crystallinity of both hot-press compression molded (*CM*) as well as Material Extrusion Additive Manufacturing (ME-AM) samples was in all cases below 2%. Hence, this material's low crystallization ability is assumed to have an insignificant effect on the mechanical properties [7].

4.1. Isotropic bulk properties

As a first step, the mechanical properties in uniaxial compression and tensile tests were determined for the *CM* samples. These results will help to determine some initial parameters for the Ree–Eyring flow rule, and will be considered as the reference bulk behavior of the base material. The uniaxial compression test results at various strain rates are shown in Fig. 3. The stress–strain curves are the average values of three compression test results. Measurements have good repeatability as standard deviation stays below 0.95 MPa (see also Table A.1). As is indicated in Fig. 3(a), at the highest strain rate $\dot{\varepsilon} = 1 \cdot 10^{-1}$ s^{-1} the sample was affected by viscous heating at large deformations. This can be seen as a continuing reduction of the stress at higher strains, leading to a crossover with the curves at lower strain rates. Other research groups have mentioned this effect previously [46,61]. Since the Ree–Eyring flow rule does not account for viscous heating, the lower yield data point at this strain rate was not taken into account to determine model parameters.

Fig. 3(b) demonstrates the upper and lower yield stresses, and the yield drop, as a function of logarithmic nominal strain rate. The experimental upper yield data show a distinct strain-rate dependence
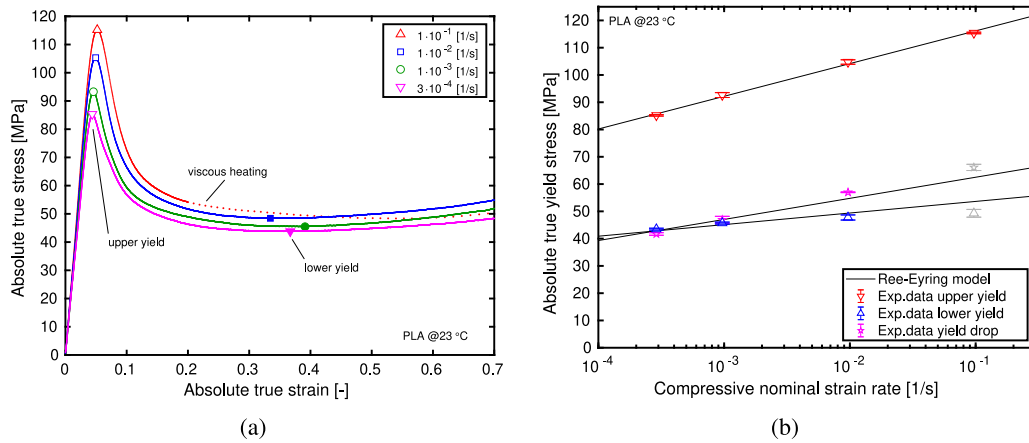
Fig. 3. (a) Experimental absolute true stress/strain response in uniaxial compression tests at various strain rates for *CM* samples. (b) Absolute true upper ($\triangledown$) and lower ($\triangle$) yield stresses, and yield drop ($\star$) as a function of logarithmic strain rate for *CM* samples. Symbols are experimental results, solid lines are model predictions. Gray symbols are data affected by viscous heating.
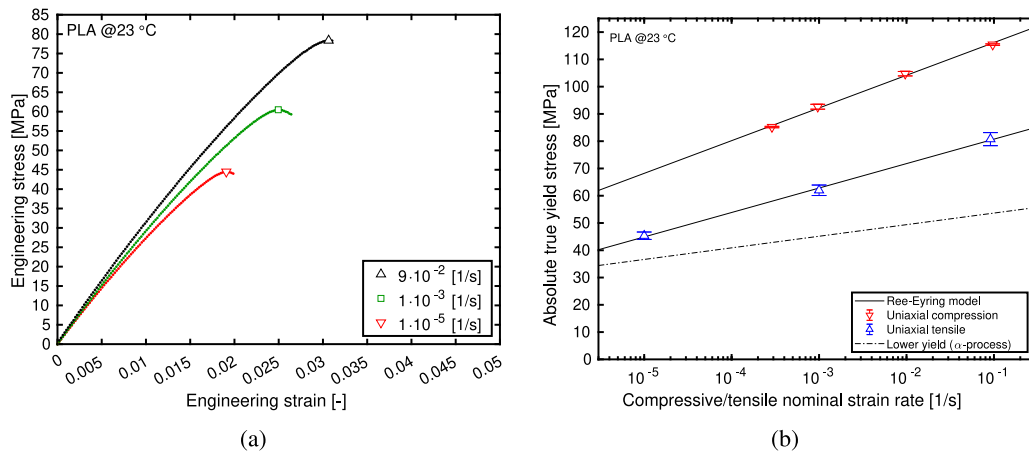

Fig. 4. (a) Experimental engineering stress/strain response in uniaxial tensile tests at various strain rates for *CM* samples. (b) Absolute true yield stresses as a function of logarithmic strain rate for *CM* samples. Symbols are experimental results, solid lines are model predictions. The dash–dotted line is the model prediction of the compression lower yield stress, which is related to the α-process only.

compared to the lower yield stresses. According to the method published by Van Breemen et al. [46], this is an indication of the material's thermorheologically complex behavior. And indeed, the PLA material used in the present study can be adequately described with 2 molecular deformation processes. This was already suggested previously [7], but not experimentally demonstrated using uniaxial compression tests. Similar behavior was found for another PLA grade [46]. The primary relaxation process, associated with the glass transition and indicated as the α-process, is assigned to cooperative local segmental motions. The secondary or β-relaxation process is thought to be related to non-cooperative local twisting motions of the main chain [62–64].

Analogous to the PLA used in the Van Breemen study [46], the present PLA material also shows a pronounced strain softening response followed by weak strain hardening (see Fig. 3(a)). Such behavior generally leads to brittle behavior in uniaxial tensile tests. This is confirmed by the uniaxial tensile test results at various strain rates, as shown in Fig. 4(a). The stress–strain curves are the average values of three tensile test results. On the other hand, the tensile test specimens show some weak stress-whitening due to the appearance of white lines perpendicular to the tensile direction distributed over the gauge length of the specimen. These lines are attributed to the crazing behavior of the PLA material [65,66], and similar to what is seen for polystyrene.

Fig. 4(b) displays the true compressive and tensile yield stresses as a function of logarithmic nominal strain rate. It can be clearly seen that the strain-rate dependence for the compressive yield stresses is

Table 4
Ree–Eyring model parameters for PLA material of *CM* samples.

x	μ_x [–]	V_x^* [nm³]	ΔU_x [a] [kJ mol⁻¹]	$\dot{\gamma}_{0,x}^{comp}$ [s⁻¹] (lower yield)	$\dot{\gamma}_{0,x}^{comp}$ [s⁻¹] (yield drop)	$\dot{\gamma}_{0,x}^{tens}$ [s⁻¹]
α	0.25	4.48	480	$3.81 \cdot 10^{71}$	–	$3.18 \cdot 10^{73}$
β	0.25	2.46	100	–	$1.25 \cdot 10^{9}$	$1.25 \cdot 10^{9}$

[a] Data taken from Van Breemen et al. [46].

higher than for the tensile yield stresses. The tensile data demonstrate a slope of ±9 MPa/decade, while the compression data manifest a slope of ±12 MPa/decade (similar to but slightly lower than measured by Engels et al. [42] and Van Breemen et al. [46]). This effect is due to the influence of the hydrostatic pressure [45,58,60]. And it is used to determine the hydrostatic pressure parameter μ_x [45]. For illustrative reasons, Fig. 4(b) also shows the model prediction of the compressive lower yield stress, which is only determined by the primary (α) molecular deformation process. Note that the strain-rate dependence of the α-process is different from the tensile yield stress, which is governed by both the α- and β-processes.

By making use of the methodologies as explained by Van Breemen et al. [46] and Verbeeten et al. [45], the Ree–Eyring parameters for Eqs. (7) and (8) can be determined. Table 4 gives these parameters, while the solid lines in Figs. 3 and 4 show the predictive capacity

of the model. Since the transition from the (α) towards the ($\alpha + \beta$) contribution is not manifested neither in the tensile nor in the upper yield compression data, the pressure dependence parameter μ_x cannot be determined separately for each molecular deformation process [45] and is taken equal for both processes. Take also into account that when the material shows a combined behavior of both the α- and the β-process, the values for the $\dot{\gamma}_{0,\alpha}$ and $\dot{\gamma}_{0,\beta}$ parameters are not unique.

From a practical point of view, the activation volume of the α-relaxation process V_α^* determines the slope of the lower yield stress data as a function of logarithmic strain rate, while the activation volume of the β-relaxation process V_β^* determines the slope of the yield drop data. The combination of both activation volumes determines the slope of the tensile and compression upper yield stresses as a function of logarithmic strain rate. The pressure dependence parameter μ determines the difference in strain-rate dependency between the tensile and compression yield stress data. And last, the $\dot{\gamma}_{0,x}$-parameters determine the height of the yield stress curves.

4.2. Angle-ply ME-AM samples

Compression molded samples, which are completely solid, are isotropic in nature. Its properties are mostly determined by the temperature and pressure profiles as a function of time, *i.e.* $T_{CM}(t)$ and $p_{CM}(t)$. This leads to a certain thermodynamic state of the amorphous phase and a specific amount of crystallinity (negligible for the current material [7]). Due to its isotropy, *CM* samples are considered as the material's reference mechanical behavior in the present study.

On the contrary, Material Extrusion Additive Manufacturing (ME-AM) samples consist of stacked layers of partially bonded filaments with interstitial voids [9,16]. Pressure drops to atmospheric levels once the material exits the nozzle. The temperature profile is highly non-isothermal due to the initial fast cooling and successive heating cycles during the consecutive deposition of strands. And shear effects in the nozzle and due to the curvature between nozzle and deposited strand will lead to orientation and stretch of the polymer chains [11, 13,67]. Hence, mechanical properties are anisotropic and determined by a significantly different thermo-mechanical history, *i.e.* $T_{AM}(t)$ and $\dot{\gamma}_{AM}(t)$.

Furthermore, the ME-AM voided structure has an influence on the measured stress–strain curves, as voids lower the stress values. To be able to compare different 3D printed sets, which generally have a variation in porosity, between each other and with the *CM* sample set, the voided structure is compensated using Eq. (3) to obtain "void corrected" or "solid" yield stress results. Thus, the effect of the infill orientation stacking sequence can be determined in a macroscopic sense.

The stress–strain results for the symmetric angle-ply ME-AM sample sets are given in Fig. 5 Results for the *quasi-isotropic* set is also shown in Fig. 5. Average porosities and apparent densities for each set are given in Table 5. The shown stress–strain curves are average curves of three tensile test results. In the subfigures on the right, the directly measured yield stresses are indicated with open symbols, while the *void corrected* results are displayed by closed symbols.

As was also shown previously [7], it immediately draws the attention that with the current printing parameters all ME-AM sample sets show significantly more ductile behavior than the *CM* sample set (2.6% strain at break for the *CM* sample, and ranging from 3.1% to 6.6% for the ME-AM samples at a strain rate of $\dot{\varepsilon} = 10^{-3}$ s^{-1}; see also Table A.2). This is a clear effect of the ME-AM processing step. Additionally, ductility seems to be higher for the intermediate infill orientations, *i.e.* sample set *PLAo45* and *PLAo60*. Stress-whitening in the form of white lines perpendicular to the tensile force direction are observed in all test samples. The amount of stress-whitening, however, is higher than for the *CM* test samples. Furthermore, samples which show higher strain-at-break also exhibit more stress-whitening. This indicates that multiple craze formation seems to be the failure mechanism for this

Table 5
Average apparent density, porosity, and dimensional length change of ME-AM samples. Standard deviations are indicated between brackets.

Sample nomenclature	$\bar{\rho}_{app}$ [g cm^{-3}]	Porosity [%]	Length [%]
PLAo00	1.12 (0.009)	10.1 (0.7)	−12.8 (0.9)
PLAo15	1.17 (0.009)	6.6 (0.8)	−8.8 (0.8)
PLAo30	1.16 (0.006)	7.5 (0.5)	−7.2 (0.5)
PLAo45	1.16 (0.006)	7.0 (0.5)	−5.8 (0.7)
PLAo60	1.16 (0.007)	7.2 (0.5)	−4.2 (0.2)
PLAo75	1.14 (0.004)	9.1 (0.3)	−3.2 (0.1)
PLAo90	1.15 (0.006)	7.8 (0.4)	−3.3 (0.1)
PLAoISO	1.14 (0.005)	8.5 (0.4)	−5.5 (0.6)

Table 6
Model parameters used to describe the yield behavior of Compression Molded (*CM*) and ME-AM samples. Pressure dependence parameters are taken as $\mu_\alpha = \mu_\beta = 0.25$. Activation energies are taken as $\Delta U_a = 480$ kJ mol^{-1} and $\Delta U_b = 100$ kJ mol^{-1} [46].

| Sample nomenclature	V_α^* [nm^3]	$\dot{\varepsilon}_{0,\alpha}$ [s^{-1}]	V_β^* [nm^3]	$\dot{\varepsilon}_{0,\beta}$ [s^{-1}]
CM	4.48	$3.92 \cdot 10^{68}$	2.46	$6.23 \cdot 10^{11}$
PLAo00	4.48	$2.49 \cdot 10^{62}$	2.46	$5.95 \cdot 10^{14}$
PLAo15	4.48	$4.90 \cdot 10^{62}$	2.46	$1.28 \cdot 10^{15}$
PLAo30	4.48	$5.81 \cdot 10^{62}$	2.46	$1.62 \cdot 10^{15}$
PLAo45	4.48	$5.39 \cdot 10^{62}$	2.46	$2.14 \cdot 10^{15}$
PLAo60	4.48	$9.80 \cdot 10^{62}$	2.46	$2.10 \cdot 10^{15}$
PLAo75	4.48	$4.63 \cdot 10^{63}$	2.46	$2.43 \cdot 10^{15}$
PLAo90	4.48	$4.55 \cdot 10^{63}$	2.46	$2.98 \cdot 10^{15}$
PLAoISO	4.48	$9.92 \cdot 10^{62}$	2.46	$3.45 \cdot 10^{15}$

PLA material [65,66], also holding up for ME-AM processed samples. The SEM fractography section will provide more details on the fracture mechanism.

The calculated apparent densities of the current sample sets are lower than the ones calculated in the previous study [7]. As a consequence, sample porosities are higher. While in the previous study all average porosities were below 6% [7], in the present research values range between 6.6% and 10.1%. Although the same printer parameters are used, a different printer is employed, which has its effect on the measured results. Nevertheless, the trends shown by the results are very similar.

The strain-rate dependence of the yield stresses for these ME-AM sample sets can be adequately captured using the pressure-dependent Ree–Eyring modification of the Eyring-type flow rule as given by Eq. (7). The model predictions are shown in the subfigures on the right of Fig. 5 as black solid lines. Model parameters are given in Table 6. Excellent model descriptions are obtained, especially taken into account that the same activation volumes for the α- and β−relaxation processes as determined from the *CM* sample results are used for all ME-AM sample sets (see Table 6). The coefficient of determination R^2 is for all sets above 0.98, demonstrating the outstanding correlation between experiments and model. Except for set *PLAo90*, where the coefficient of determination drops slightly to $R^2 \approx 0.95$, still manifesting a satisfying fit.

Note that the values for the rate constants $\dot{\varepsilon}_{0,\alpha}$ and $\dot{\varepsilon}_{0,\beta}$ of the *CM* sample set in Table 6 are different from the values given in Table 4. The rate constant for the α-deformation process is lower, while it is higher for the β-process. However, the model performance is completely equal for both parameter sets. This confirms the argument that values for the rate constants are not unique, if no distinction can be made between both deformation processes.

Also remarkable is the distinct change in slope of the strain-rate dependence of the yield stress in Fig. 5. The ME-AM sample results evidently show a transition from a low strain-rate region with only the contribution from a single deformation process (α) towards a high strain-rate region with contributions of two deformation processes ($\alpha + \beta$). This clear transition is not detected for the compression molded tensile test specimen as shown in Fig. 4(b).
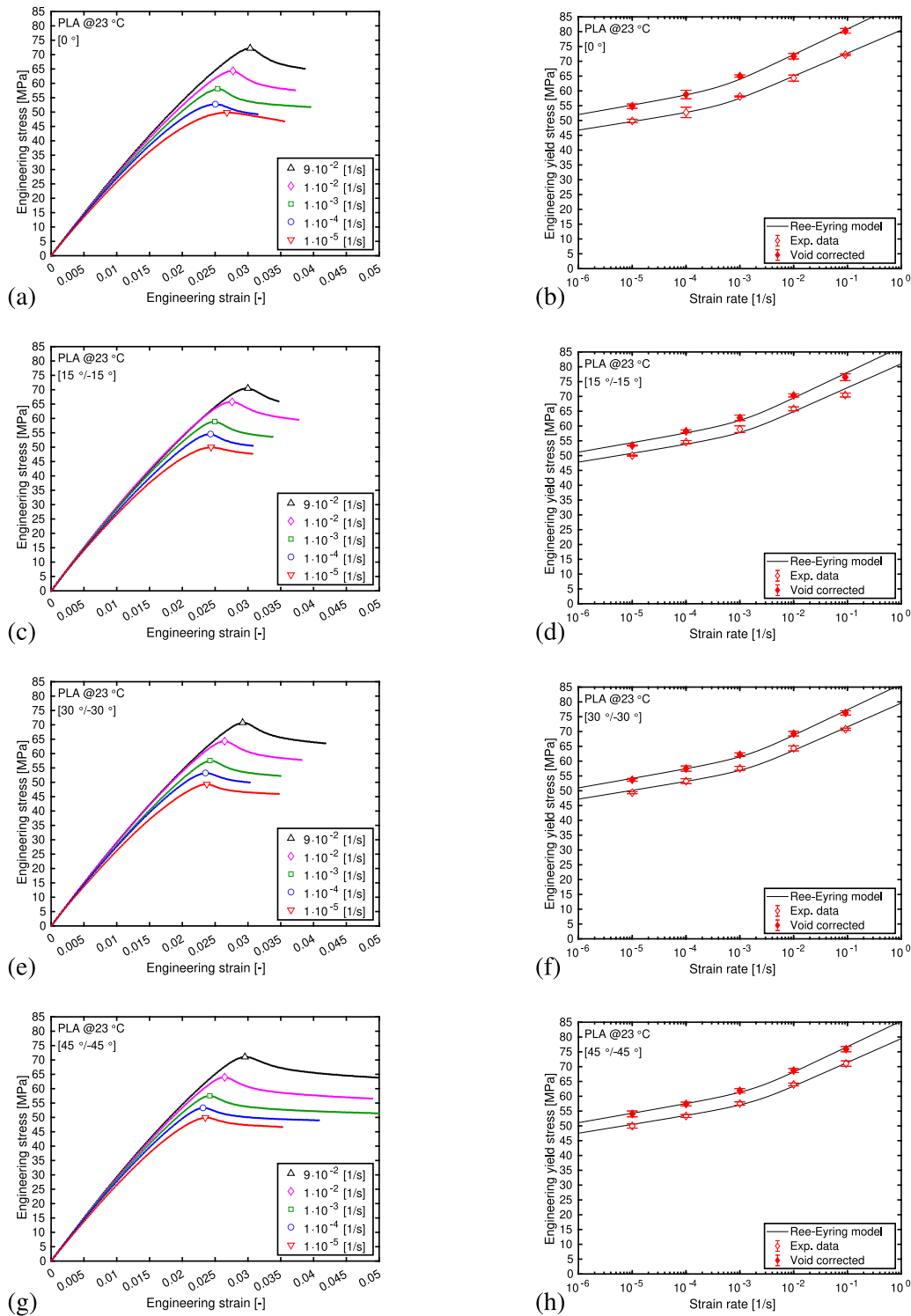
Fig. 5. Engineering stress–strain response in uniaxial tensile tests at various strain rates for ME-AM samples. *(a,c,e,g,i,k,m,o)* Stress as a function of strain. Symbols are experimental yield stresses. *(b,d,f,h,j,l,n,p)* Yield stress and void corrected yield stress as a function of logarithmic strain rate. Symbols are experimental results, solid lines are model predictions. *(a,b)* [0°], *(c,d)* [15°/−15°], *(e,f)* [30°/−30°], *(g,h)* [45°/−45°], *(i,j)* [60°/−60°], *(k,l)* [75°/−75°], *(m,n)* [90°], *(o,p)* [0°/90°/45°/−45°].

Although a transition from an α-region towards an $\alpha + \beta$-region was also suggested in the previous study [7], experimental evidence was less clear. The reason may be that a relatively low number of strain rates was applied. Here, more strain rates are measured over the same strain-rate range, and the transition has become more apparent. A plausible explanation for this transition is suggested in the next subsection.

4.3. Orientation induced anisotropy

Several research groups have mentioned, reasoned, and measured that the ME-AM processing technique induces local orientation and stretch of the molecular chains [7,11,13,16,18,67,68]. It was also previously shown that variations in molecular chain orientation and stretch
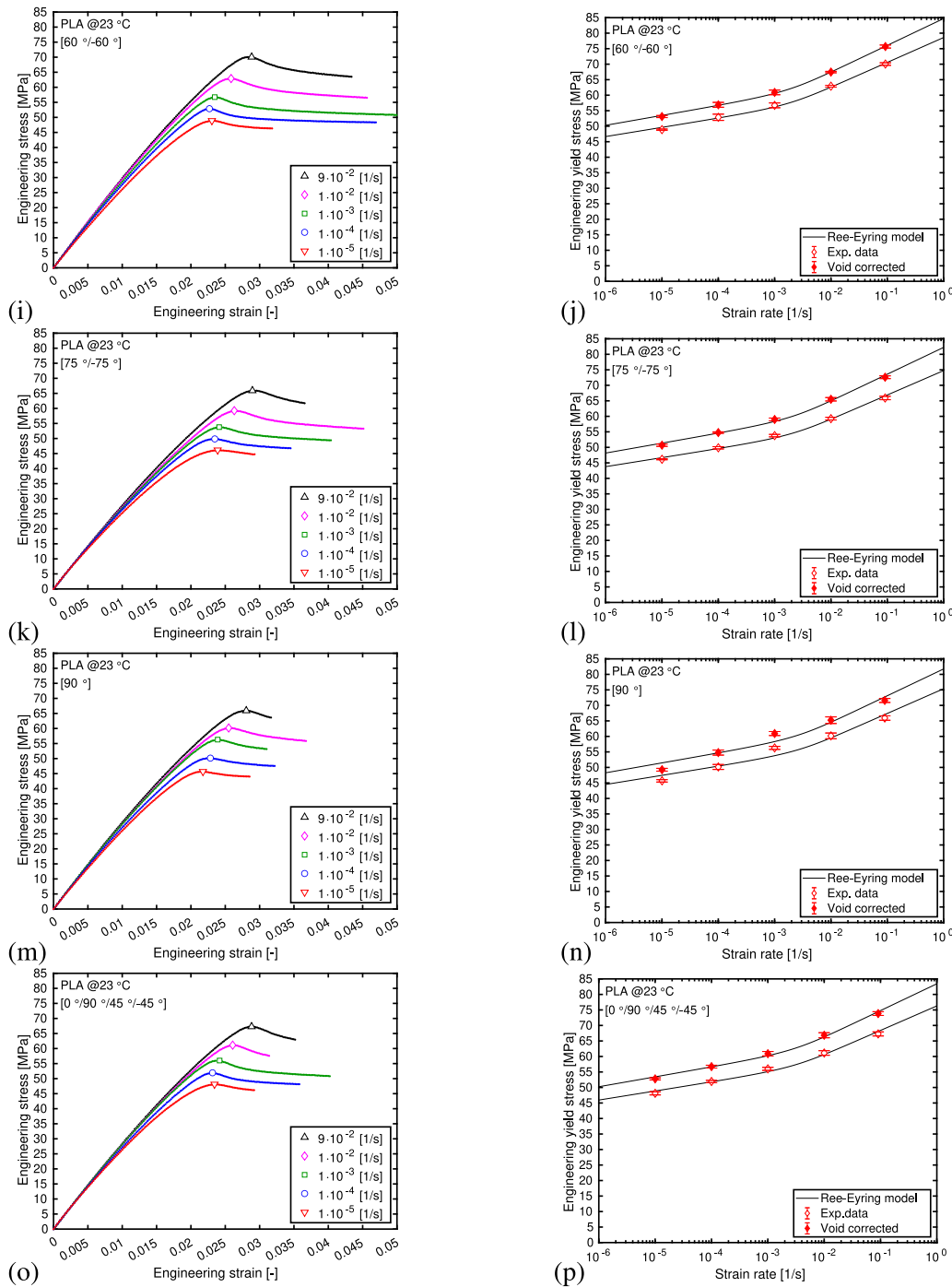
Fig. 5. (*continued*).

produce changes in mechanical properties, both for ME-AM components [7,16], as well as oriented polymers due to hot drawing [69,70], hydrostatic extrusion [69,71], or even injection molding [53,54].

Using a thermal shrinkage procedure [7,16], a qualitative macroscopic measurement for molecular orientation and stretch can be determined. Dimensional variations are due to, on the one hand, cold crystallization and, on the other hand, relaxation of the residual chain alignment. As explained in Section 2.6, the variations in dimensional changes are an indication for the molecular chain relaxation.

Table 5 shows the average dimensional length changes of the various ME-AM sample sets. Logically, the *PLAo00* set has the highest

length contraction (12.8%), as the deposited polymer strands are oriented completely in the sample length direction. Augmenting the orientation angle from [0°] to [90°] reduces this length change, towards the minimum of 3.2% contraction for both *PLAo75* and *PLAo90* sets. The quasi-isotropic *PLAoISO* sample set has a contraction close to but slightly lower than the *PLAo45* sample set. Therefore, the most pronounced effect on the mechanical properties, compared to the *CM* samples, should be visible for the *PLAo00* sample set, as the tensile forces are imposed in the direction of the deposited strands.

Fig. 6 compares the strain-rate dependence of the (*void corrected*) yield stress between the *CM* and *PLAo00* sample sets. It can be easily seen that the contribution of the α-deformation process has increased
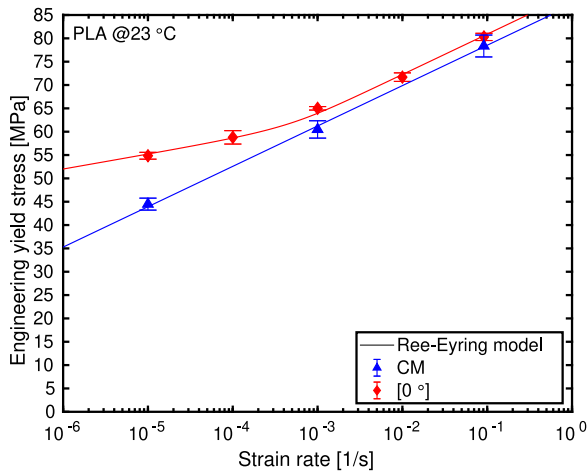
Fig. 6. Yield stress and *void corrected* yield stress as a function of logarithmic strain rate for the *CM* and *PLAo00* sample sets. Symbols are experimental data, lines are model predictions.

significantly for the *PLAo00* samples compared to the *CM* set. As a consequence, only this α-relaxation process becomes noticeable at low strain rates, while both molecular relaxation processes ($\alpha + \beta$) become visible at higher strain rates. An ($\alpha \rightarrow \alpha + \beta$)-transition is provoked for the *PLAo00* sample set, which is not detected for the *CM* sample set. When the rate constants $\dot{\varepsilon}_{0,\alpha}$ and $\dot{\varepsilon}_{0,\beta}$ from Table 6 are compared, the $\dot{\varepsilon}_{0,\alpha}$ parameter diminishes for *PLAo00*, while $\dot{\varepsilon}_{0,\beta}$ increases. This implicates that the primary α-process, assigned to cooperative local segmental motions of the molecular backbone, is hindered, whereas the secondary β-process, related to non-cooperative local twisting motions of the main chain, becomes somewhat easier. Hence, it is suggested that the oriented and extended molecular chain as a result of the ME-AM processing step (note the 12.8% length contraction for this sample set in Table 5), hampers the α-deformation process of the molecular backbone. As a consequence of this reduced molecular mobility, yield stresses related to that primary relaxation process increases. Subsequently, deformation related to the β-process is slightly favored and yield stresses, attributed to this secondary process, diminish. A similar response was indicated by Senden et al. [72] for oriented polycarbonate (PC).

As the orientation angle is increased, the chain orientation and extension rotates away from the axis of the tensile forces during mechanical characterization (compare the length contraction data in Table 5). To show how it affects the yield stresses, the ME-AM sample sets at different infill orientations are compared in Fig. 7(a). All sets still show the transition from the α-relaxation towards the ($\alpha+\beta$)-relaxation. However, curves move down and to the right at increasing infill orientation angle. Although still hindered, molecular chain deformation seems to become easier at increasing angle. As a consequence, the rate constants for the α- and β-processes slowly increase, as the values from Table 6 indicate.

Senden et al. [72], in a study on oriented polycarbonate and in a subsequent study on oriented polyethylene (PE) [54], explored and modeled anisotropy in oriented polymers by focusing on loading angle and strain rate. Their model featured two sources of anisotropy: a frozen-in elastic network stress due to initial material orientation in combination with an anisotropic viscoplastic flow rule based on a Hill yield function. A frozen-in internal stress, as a consequence of a pre-stretched elastic network, provokes increased strain hardening in tensile tests. Such effect may also explain the more ductile behavior of ME-AM processed samples in the tensile test experiments of the present study. Furthermore, the behavior shown in Fig. 7(a) displays similar tendencies and features as results from Senden et al. [54].

Therefore, their model may well be applied to the present study. For that, however, a complete three-dimensional model is necessary. This is, though, outside the scope of the present study.

To explore how the *quasi-isotropic* sample set relates to the other ME-AM samples, Fig. 7(b) compares set *PLAoISO* to the set with the highest *volume corrected* yield stresses, *i.e.* set *PLAo00*, and to the set with the lowest values, set *PLAo90*. Since set *PLAoISO* has strands oriented in four different directions, it combines mechanical properties of symmetric angle-ply laminate configurations [0°], [90°], and [45°/−45°]. Thus, it logically demonstrates yield stresses in between the other two sets.

As can be concluded from Table 6, the ME-AM sample sets with different infill orientation angles can be adequately described with a Ree–Eyring flow rule using 2 fixed activation volumes (as determined on *CM* processed samples) and changing rate constants. To analyze these rate constants, both $\dot{\varepsilon}_{0,\alpha}$- and $\dot{\varepsilon}_{0,\beta}$-parameters are shown as a function of the infill orientation angle in Fig. 8. Fig. 8(a) demonstrates that the rate constant related to the α-process stays almost constant at both low and high infill orientation angles. In between, at around approximately 65°, the plot exhibits a kind of "jump" from a lower to a higher value. On the other hand, Fig. 8(b) seems to reveal a steady increase of the $\dot{\varepsilon}_{0,\beta}$-parameter below an infill orientation angle of 60°, followed by a slower change at higher orientation angles. This insinuates that at lower orientation angles, it is easier for the material to deform due to twisting motions instead of local segmental motions. At higher orientation angles, when the oriented and stretched polymer is rotated far enough away from the tensile force axis, the cooperative local segmental motions start to play a more important role in the material's deformation dynamics.

If the tendencies as shown in Fig. 8 are taken into account for the rate constants in the Ree–Eyring modification of the Eyring flow rule (*i.e.* the dashed lines), the yield stresses at different strain rates and as a function of orientation angle can be predicted. Fig. 9 shows the predictions at a lower strain rate and at a higher strain rate. At the strain rate of $\dot{\varepsilon} = 10^{-4}$ s^{-1}, mostly the α-relaxation process is active. At the higher strain rate of $\dot{\varepsilon} = 10^{-2}$ s^{-1}, both deformation processes act. For the lower strain rate, yield stresses are slightly underpredicted. However, the tendency of the yield stress as a function of orientation angle is clearly well captured. For the higher strain rate, yield stresses are excellently modeled. The other strain rates, although not shown here, slightly over- or underpredict the yield stress values, similar to Fig. 9(a). Nevertheless, the trend is definitely well captured. Note that the range of the *y*-axes in Fig. 9 is smaller than for Fig. 5, which enlarges the differences between the measured data and the model.

As can be concluded from the previous results, this PLA material manifests a deformation-dependent Eyring rate constant. Its activation volumes for the two relaxation processes can be adequately determined on compression molded samples for tensile and compression characterization tests and do not seem to change due to different processing techniques. The rate constants, however, are determined by the thermo-mechanical history (*i.e.* time–temperature and time–strain profiles) the material undergoes during the ME-AM process. This was also concluded in a previous study [7]. Nevertheless, this does not hold for all ME-AM processed materials. For example, it was shown that ME-AM processed ABS rather shows a deformation-dependent activation volume [18].

4.4. SEM fractography

Following uniaxial tensile testing, the fracture surface of the as-received filament, hot-press compression molded specimens, and material extrusion additive manufactured test samples were observed using scanning electron microscopy. Observations provide additional insight on the fracture mechanism for this PLA material.

The as-received PLA filament was characterized under tension at a strain rate of $\dot{\varepsilon} = 10^{-2}$ s^{-1} until failure. A cross-section of the filament's fractured surface was analyzed by SEM micrography and is shown in
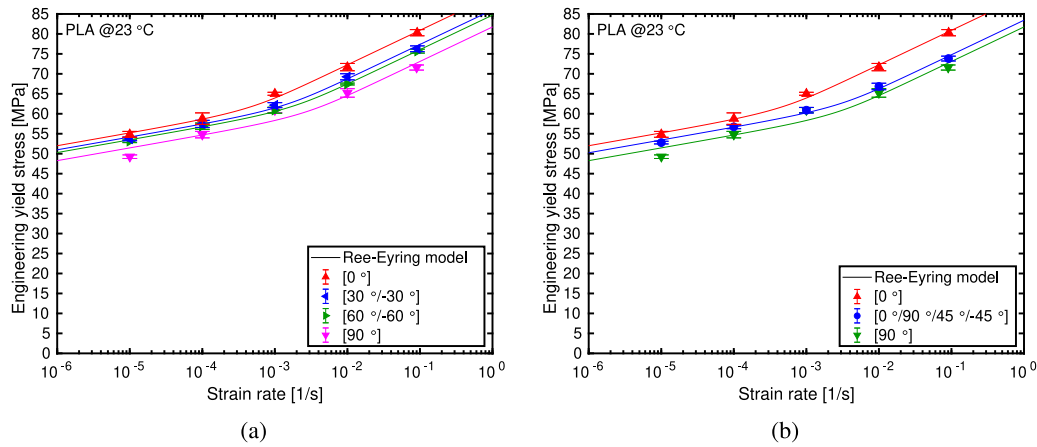
Fig. 7. (a) *Void corrected* yield stress as a function of logarithmic strain rate for various ME-AM sample sets. (b) *Void corrected* yield stress as a function of logarithmic strain rate for the *quasi-isotropic* ME-AM sample set compared to *PLAo00* and *PLAo90*. Symbols are experimental results, solid lines are model predictions.
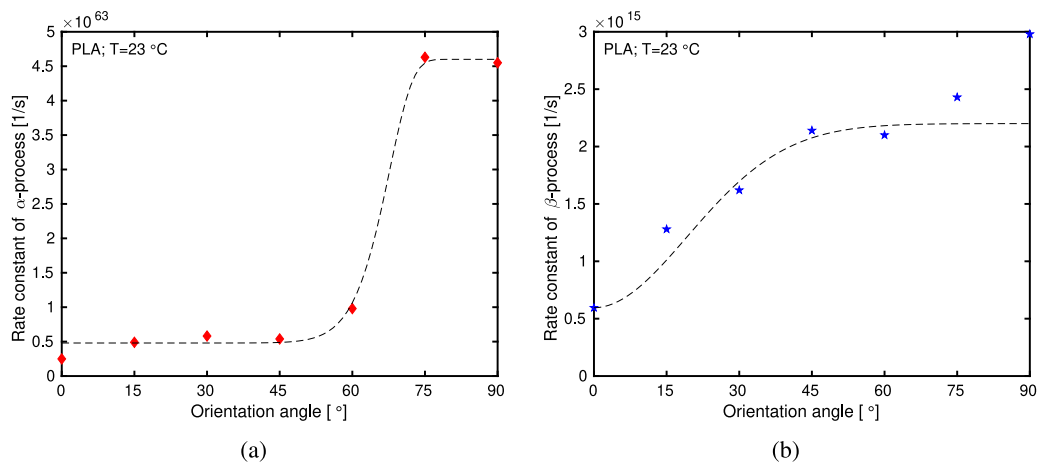

Fig. 8. Rate constant $\dot{\varepsilon}_0$ as a function of infill orientation angle. (a) Related to α-relaxation process. (b) Related to β-relaxation process. Symbols are values from Table 6, dashed lines are a guide to the eye.
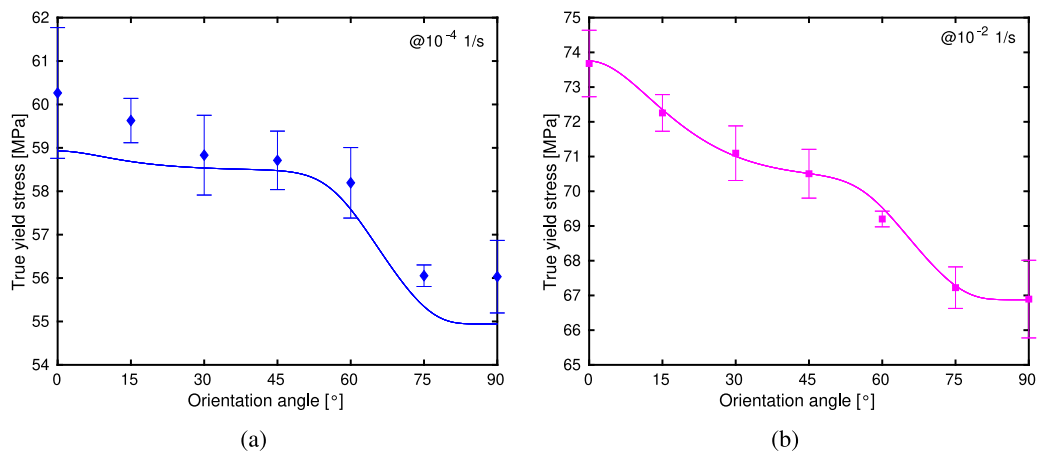

Fig. 9. *Volume corrected* true yield stress as a function of infill orientation angle. (a) For strain rate $\dot{\varepsilon} = 10^{-4}$ s^{-1}. (b) For strain rate $\dot{\varepsilon} = 10^{-2}$ s^{-1}. Symbols are experimental values, solid lines are model predictions.

Fig. 10. The filament fractures in a macroscopically brittle manner, as can be deduced from Fig. 10(a). The surface is rather smooth and only few plastically deformed regions can be seen, indicated by white zones/lines. These are, however, very localized. Especially the filament border demonstrates these plastic deformation zones, as shown in Fig. 10(b).

At magnifications of 200x and higher very thin lines of material become visible, which are highly extended micro-fibrils. These can be detected, among others, near the tip of the green arrow in Fig. 10(b). At a higher magnification, see Fig. 10(c), such a micro-fibril has recoiled onto the surface. As this image shows, one end of the extended material is attached to the surface and shows high ductile tearing, while the
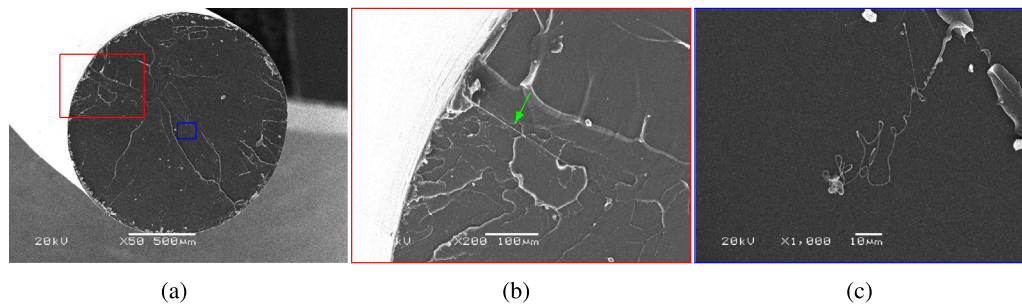
Fig. 10. SEM micrographs of the as-received PLA filament cross-section. (For interpretation of the references to color in this figure legend, the reader is referred to the web version of this article.)
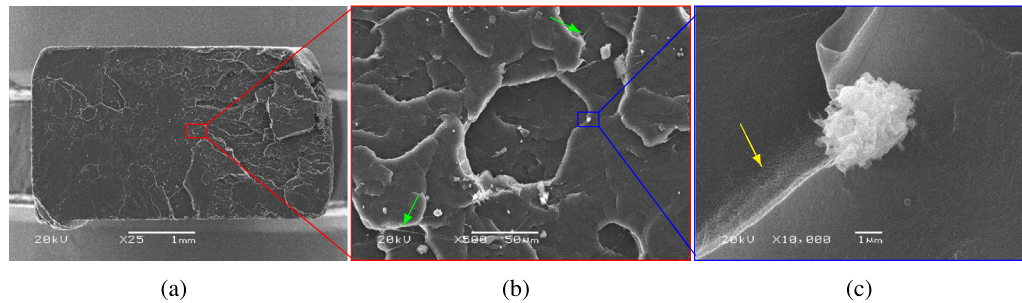

Fig. 11. SEM micrographs of the *CM* PLA sample fracture cross-section. (For interpretation of the references to color in this figure legend, the reader is referred to the web version of this article.)
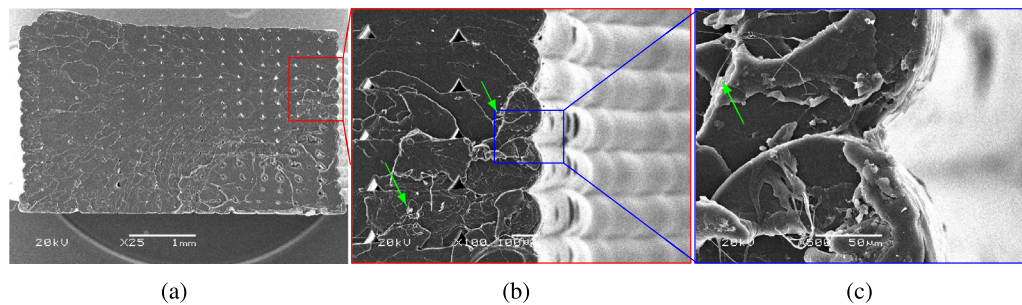

Fig. 12. SEM micrographs of the ME-AM *PLAo00* sample fracture cross-section, [0°]. (For interpretation of the references to color in this figure legend, the reader is referred to the web version of this article.)

other end is lying loose on the surface. This seems to suggest that micro-fibrils start during mechanical characterization, are extended during the test, and break at the moment of sample fracture. Hence, as was suggested by Jiang et al. [73], it seems likely that these micro-fibrils are formed during crazing of the material.

In Figs. 11 to 15, SEM micrographs of the fracture surfaces of arbitrary samples for the different sample sets are displayed. All shown samples were mechanically characterized at a strain rate of $\dot{\varepsilon} = 10^{-2}$ s^{-1}, except for the *CM* sample, which was tested at $\dot{\varepsilon} = 10^{-3}$ s^{-1}. Although not shown here, no significant variations on the fracture surfaces were observed for samples that were tested at other strain rates.

A cross-section of a mechanically characterized *CM* PLA sample analyzed by SEM micrography is shown in Fig. 11. The left half of the fractured sample demonstrates a more brittle fracture surface with rather few white zones (related to plastic deformation), as shown in Fig. 11(a). On the other hand, the right half shows more intense white stripes indicating more plastically deformed regions. The fracture surface is still typical for brittle fracture, though. The direction of the white lines on the right half seem to indicate that the fracture initiated on the left side of the sample. Note that Fig. 4(a) manifests macroscopically brittle behavior for this sample set.

At a higher magnification, *i.e.* Fig. 11(b), some micro-fibrils become visible (near the tip of the green arrows), similar to the PLA filament images. Although there are some zones with a higher amount of micro-fibrils, the density of micro-fibrils is rather low on this *CM* sample fracture surface, compared to the ME-AM surfaces. As mentioned before, these micro-fibrils are thought to be related to crazing behavior [66,73].

In Fig. 11(c), a high magnification of 10,000x is shown. Apart from the white zone with local plastic deformation, small micro-cracks are visible near the tip of the yellow arrow. Although Fig. 11(c) suggests that they seem to be present in a large portion of the fracture surface, these micro-cracks only become visible at this high magnification of 10,000x. It is suggested that these micro-cracks are the reason for the stress-whitening seen in the gauge section of the tensile test specimen at a macroscopic scale, and, hence, thought to be related to crazing.

The images related to the surfaces of ME-AM processed samples, Figs. 12 to 15, all show brittle surface fracture. But, the amount of plastic deformation (white zones) is higher compared to the *CM* sample. Figs. 12(b) and 12(c) more clearly show that the white zones are related to local ductile tearing of the material.

Especially in Fig. 12, which displays representative SEM images of the fracture surface of an ME-AM *PLAo00* sample, triangular-shaped inter-strand and inter-layer voids can be easily detected. A few voids,
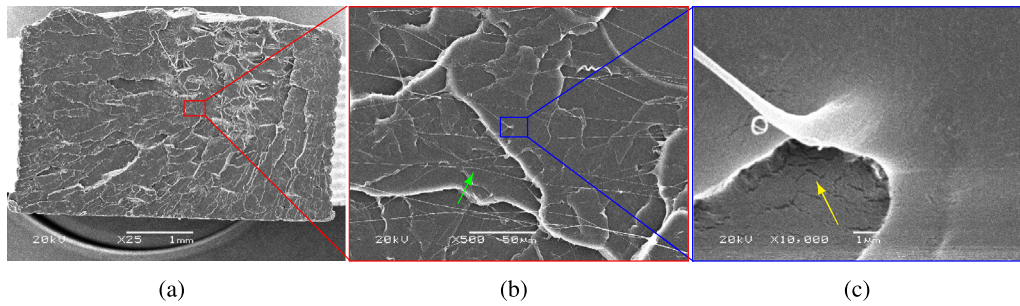
Fig. 13. SEM micrographs of the ME-AM *PLAo60* sample fracture cross-section, [60°/−60°]. (For interpretation of the references to color in this figure legend, the reader is referred to the web version of this article.)
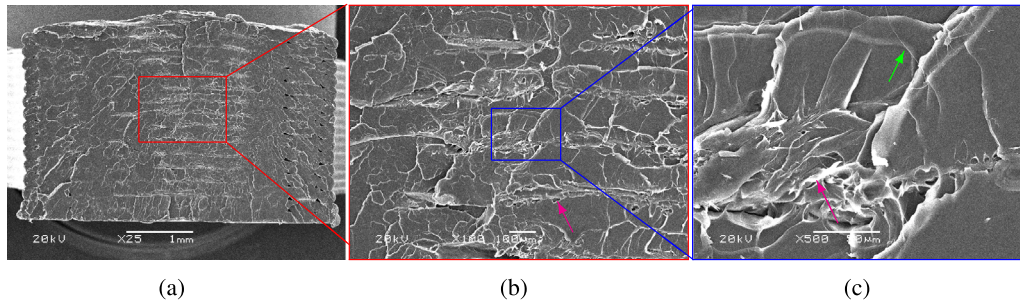

Fig. 14. SEM micrographs of the ME-AM *PLAo90* sample fracture cross-section, [90°]. (For interpretation of the references to color in this figure legend, the reader is referred to the web version of this article.)
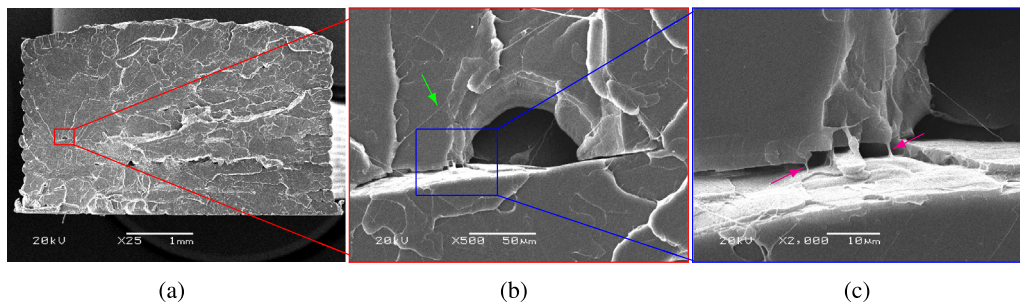

Fig. 15. SEM micrographs of the ME-AM *PLAoISO* sample fracture cross-section, [0°/90°/45°/−45°]. (For interpretation of the references to color in this figure legend, the reader is referred to the web version of this article.)

notwithstanding, are also visible in the perimeters of the other ME-AM samples. The triangular voids are relatively small, and occasionally almost absent. This indicates an adequate choice of ME-AM processing parameters to obtain good adhesion between strands and layers. The adhesion widths and heights are substantial, again confirming good adhesion quality. Consequently, good mechanical properties are achieved.

Also on the ME-AM fracture surfaces, micro-fibrils can be detected, some of which are marked by the green arrows. The amount of micro-fibrils is higher than seen on the surface of the *CM* sample, especially near regions with higher local plastic deformation. Particularly Fig. 13(b) shows a high amount of micro-fibrils. Since these *PLAo60* samples also present high levels of stress-whitening and Fig. 5(i) demonstrates relatively high strain-at-break for this sample set, it seems to indicate that the amount of micro-fibrils is related to sample ductility. In agreement with this idea is the lower density of micro-fibrils for the *PLAo90* sample shown in Fig. 14(c). That sample set also demonstrates a lower strain-at-break, as shown in Fig. 5(m).

Previous publications [22,74,75] have also detected micro-fibrils on the fracture surface of ME-AM processed specimen. Yet, there was no mention of them in two of these studies [22,75], while Wittbrodt et al. [74] only indicated them as *string-like artifacts*.

In Fig. 13(c), the *PLAo60* sample also reveals micro-cracks near the tip of the yellow arrow, similar to the *CM* sample. They only become visible at high magnifications of 10,000x and are thought to be related to the macroscopic stress-whitening and crazing, as mentioned previously.

Both *PLAo90* and *PLAoISO* samples have [90°] configuration layers. Some of these layers show incomplete adhesion, see Figs. 14 and 15. A close-up of several incomplete fused lines are displayed in Fig. 14(b) for a *PLAo90* sample, demonstrating a void at the tip of the magenta arrow. In Fig. 14(c), high local ductile tearing near the magenta arrow located at an adhesion line between layers can be seen. For the *PLAoISO* sample (see Fig. 15(a)), particularly between the fourth and fifth layer, a line is visible with relatively large voids. Figs. 15(b) and 15(c) show close-ups of a larger void on top of an incomplete layer adhesion. It can be seen that there is still some connection along the weak adhesion layer due to local bridging, marked by the magenta arrows. Despite the fact that adhesion seems weak, high local deformation and bridging still give the layer adherence some strength.

The results shown in this subsection indicate that the fracture surfaces of both *CM* and ME-AM samples show brittle fracture behavior. White zones of local plastic deformation on the fracture surface are more present in samples that show higher strain-at-break. Furthermore, it seems that the presence of micro-fibrils, which are thought to be

formed during crazing [66,73], is also related to macroscopic ductility. In any case, stress-whitening (due to craze-formation) is attributed to strain-at-break, as it increases with higher sample ductility.

5. Conclusions

The effect that different infill orientation angles have on the strain-rate dependence of Material Extrusion Additive Manufactured (ME-AM) tensile test samples made with PolyLactic Acid (PLA) was investigated and analyzed. Symmetric angle-ply stacking sequences were adopted to fabricate the various ME-AM sample sets, from 0° to 90° in 15° increments. Measured yield stresses were compensated for the voided structure, typical of ME-AM components, by using apparent densities. In this way, a comparison between "solid" tensile samples could be applied. Hence, the influence of the processing step on the macroscopic material behavior could be determined. Furthermore, molecular orientation and stretch was macroscopically assessed by a thermal shrinkage procedure. Hot-press compression molded samples were also manufactured and mechanically characterized in uniaxial compression and tensile tests. These were used to determine bulk properties and initial model parameters, which have been compared to the ME-AM sample sets. Finally, a *quasi-isotropic* ME-AM sample set was also used for comparison.

All ME-AM samples show (semi-)ductile tensile behavior, contrary to the hot-press compression molded (*CM*) specimens, which display macroscopically brittle fracture. Additionally, the ME-AM specimens demonstrate a transition in the strain-rate dependence, not seen for the *CM* sample set. At low strain rates, only the contribution from the primary deformation process (α) is visible. While at high strain rates, the contribution of two deformation processes ($\alpha + \beta$) becomes evident. The *CM* sample set, however, shows no transition; its strain-rate dependence is determined by 2 molecular relaxation processes ($\alpha + \beta$). Both these effects are clearly related to the processing step, and are thought to be a result of the molecular orientation and stretch. In agreement with other studies on oriented polymers [54,72], it is suggested that the ME-AM samples provoke a pre-stretched elastic network giving rise to frozen-in internal stresses. As a consequence, oriented specimens tend to display a change in the ($\alpha \rightarrow \alpha+\beta$)-transition or changes in strain-rate dependence, and an increased strain hardening in tensile tests, which can lead to a more ductile material behavior. Yet, the compression molded PLA samples, which are isotropic and have a minimum of molecular orientation, show pronounced strain softening followed by weak strain hardening. This type of behavior is responsible for brittle fracture [42,46].

Anisotropy is detected for the ME-AM samples. The [0°] angle-ply configuration has the highest yield stresses, while yield stress behavior decreases slowly as infill orientations rotate away from the tensile force direction. The specimens with the transverse printing direction, *i.e.* the [90°] configuration, demonstrate the lowest yield stresses. Furthermore, the ($\alpha \rightarrow \alpha + \beta$)-transition in the strain-rate dependent behavior shifts to higher strain rates with increasing orientation angle. Finally, as is to be expected, the *quasi-isotropic* samples, *i.e.* with configuration [0°/90°/45°/−45°], have yield stress values in between the longitudinal printed ([0°]) and the transverse ([90°]) specimens.

The strain-rate dependence of the yield stress for both *CM* as well as ME-AM samples can be adequately described by the Ree–Eyring modification of the Eyring flow rule. This is a huge advantage, as this flow rule can be satisfactorily incorporated in accurate constitutive models [48–51,54]. Thus, this opens up the road to improve numerical structural analysis simulations for Material Extrusion Additive Manufacturing polymer components.

Initial model parameters for the Ree–Eyring flow rule were determined on the yield stress data of the *CM* sample set. From the data it was derived that this PLA material displays thermorheologically complex behavior. Data manifest a primary α-relaxation process for the lower yield compression data and a secondary β-relaxation process to

describe the yield drop data. To describe the strain-rate dependence for the ME-AM samples, the Eyring activation volumes, V_α^* and V_β^*, do not need to change. Yet, the Eyring rate constants, $\dot{\varepsilon}_{0,\alpha}$ and $\dot{\varepsilon}_{0,\beta}$, have to be adjusted to satisfactorily describe the yield stress data. Based on previous studies on oriented polymers [54,72], it is suggested that this change of the rate constants is related to the molecular orientation and stretch. Molecular chains oriented in the direction of the tensile force, as is the case for the [0°] sample set, hinders the cooperative local segmental motions of the molecular backbone (α-process) in favor of the non-cooperative local twisting motions (β-process). As the molecular orientation and stretch rotates away from the tensile force by increasing the infill orientation angle, molecular chain deformation seems to become easier and the Eyring rate constants slightly increase, in agreement with an anisotropic viscoplastic flow rule [54]. The low value for the rate constant $\dot{\varepsilon}_{0,\alpha}$, related to low molecular mobility, provokes an increase of the yield stress contribution of the primary α-process and results in the visibility of the transition from the α-region to the $\alpha + \beta$-region.

So, this PLA material demonstrates deformation-dependent Eyring rate constants, similar to what was shown for oriented PC [72]. If the tendencies for these two rate constants are taken into account in the Ree–Eyring flow rule, then yield stresses as a function of infill orientation angle can be appropriately predicted. However, this does not hold up for all polymers, since *e.g.* ME-AM processed ABS material was shown to have a strain-dependent activation volume [18].

As a last aspect, SEM microscopy was used to analyze the fracture surfaces of the as-received filament, hot-press compression molded specimens, and material extrusion additive manufactured test samples and gain insight on the fracture mechanism. All post-characterized surfaces show brittle fracture behavior. Yet, localized plastic deformation visible as whitened zones are also present. Although all samples manifest brittle surface fracture behavior, the ME-AM samples show macroscopically (semi-)ductile tensile behavior. Depending on this macroscopic ductility, localized plastic deformation zones are more or less present in SEM fractography images. Furthermore, the presence of micro-fibrils, thought to be formed during crazing [66,73], also seems to be related to macroscopic ductility. Generally, surfaces with higher amount of micro-fibrils also show higher strain-at-break. Finally, larger volumes of stress-whitening (due to craze-formation) are seen for samples with higher ductility, thus relating stress-whitening to strain-at-break.

CRediT authorship contribution statement

Wilco M.H. Verbeeten: Writing – original draft, Visualization, Validation, Supervision, Resources, Methodology, Investigation, Formal analysis, Conceptualization. **Miriam Lorenzo-Bañuelos:** Writing – review & editing, Visualization, Resources, Investigation, Conceptualization.

Declaration of competing interest

The authors declare that they have no known competing financial interests or personal relationships that could have appeared to influence the work reported in this paper.

Data availability

Data will be made available on request.

Table A.1

Average measured absolute true mechanical properties for *CM* compression test samples. Standard deviations are indicated between brackets.

Sample nomenclature	$\dot{\varepsilon}$ [1/s]	E [MPa]		Upper yield				Lower yield			
				σ_y [MPa]		ε_y [%]		σ_{ly} [MPa]		ε_{ly} [%]	
CM	$3 \cdot 10^{-4}$	2182	(14)	85.19	(0.26)	4.43	(0.05)	43.48	(0.34)	35.87	(3.41)
	$1 \cdot 10^{-3}$	2360	(70)	92.64	(0.90)	4.62	(0.06)	45.71	(0.36)	38.55	(0.80)
	$1 \cdot 10^{-2}$	2444	(196)	104.75	(0.81)	5.03	(0.14)	47.76	(0.94)	33.00	(6.12)
	$1 \cdot 10^{-1}$	2730	(21)	115.40	(0.29)	5.19	(0.01)	–	(–)	–	(–)

Table A.2

Average measured engineering mechanical properties for *CM* and ME-AM tensile test samples. Standard deviations are indicated between brackets.

Sample nomenclature	$\dot{\varepsilon}$ [1/s]	E [MPa]		σ_y [MPa]		ε_y [%]		ε_b [%]	
CM	$1 \cdot 10^{-5}$	2994	(190)	44.49	(1.28)	1.91	(0.16)	1.99	(0.25)
	$1 \cdot 10^{-3}$	3135	(99)	60.49	(1.86)	2.50	(0.05)	2.64	(0.12)
	$9 \cdot 10^{-2}$	3461	(173)	78.36	(2.34)	3.06	(0.05)	3.10	(0.04)
PLAo00	$1 \cdot 10^{-5}$	2798	(66)	49.85	(0.58)	2.68	(0.02)	3.55	(0.21)
	$1 \cdot 10^{-4}$	2875	(53)	52.73	(1.75)	2.50	(0.07)	3.15	(0.60)
	$1 \cdot 10^{-3}$	2950	(6)	58.12	(0.14)	2.54	(0.02)	3.95	(0.26)
	$1 \cdot 10^{-2}$	2980	(23)	64.33	(1.04)	2.77	(0.03)	3.72	(0.80)
	$9 \cdot 10^{-2}$	2986	(23)	72.20	(0.28)	3.03	(0.01)	3.87	(0.55)
PLAo15	$1 \cdot 10^{-5}$	2971	(69)	50.01	(0.16)	2.44	(0.02)	3.07	(0.18)
	$1 \cdot 10^{-4}$	2957	(21)	54.58	(0.50)	2.43	(0.02)	3.07	(0.34)
	$1 \cdot 10^{-3}$	3054	(60)	58.93	(1.12)	2.49	(0.02)	3.38	(0.36)
	$1 \cdot 10^{-2}$	3067	(36)	65.79	(0.66)	2.76	(0.03)	3.77	(0.40)
	$9 \cdot 10^{-2}$	2954	(17)	70.64	(0.66)	3.00	(0.03)	3.47	(0.41)
PLAo30	$1 \cdot 10^{-5}$	2828	(99)	49.33	(0.34)	2.37	(0.02)	3.47	(0.50)
	$1 \cdot 10^{-4}$	2955	(32)	53.24	(0.80)	2.35	(0.03)	3.03	(0.24)
	$1 \cdot 10^{-3}$	2992	(44)	57.57	(0.67)	2.42	(0.02)	3.50	(0.77)
	$1 \cdot 10^{-2}$	3062	(49)	64.30	(0.85)	2.64	(0.01)	3.82	(0.39)
	$9 \cdot 10^{-2}$	2988	(23)	70.76	(0.37)	2.92	(0.02)	4.18	(0.29)
PLAo45	$1 \cdot 10^{-5}$	2827	(29)	49.95	(0.72)	2.35	(0.04)	3.52	(0.21)
	$1 \cdot 10^{-4}$	2981	(14)	53.34	(0.49)	2.31	(0.04)	4.08	(0.18)
	$1 \cdot 10^{-3}$	3021	(52)	57.53	(0.56)	2.42	(0.02)	5.41	(0.21)
	$1 \cdot 10^{-2}$	3069	(9)	63.98	(0.48)	2.64	(0.03)	4.89	(1.41)
	$9 \cdot 10^{-2}$	3017	(18)	71.04	(0.90)	2.95	(0.02)	5.91	(0.45)
PLAo60	$1 \cdot 10^{-5}$	2874	(66)	48.90	(0.20)	2.31	(0.03)	3.18	(0.27)
	$1 \cdot 10^{-4}$	2979	(57)	52.88	(1.01)	2.27	(0.03)	4.69	(0.63)
	$1 \cdot 10^{-3}$	3057	(13)	56.73	(0.78)	2.35	(0.02)	6.62	(0.38)
	$1 \cdot 10^{-2}$	3098	(29)	62.91	(0.29)	2.59	(0.02)	4.56	(0.61)
	$9 \cdot 10^{-2}$	3027	(28)	70.05	(0.41)	2.88	(0.04)	4.34	(0.46)
PLAo75	$1 \cdot 10^{-5}$	2945	(58)	46.15	(0.17)	2.39	(0.02)	2.93	(0.14)
	$1 \cdot 10^{-4}$	2856	(52)	49.86	(0.37)	2.35	(0.02)	3.45	(0.39)
	$1 \cdot 10^{-3}$	2915	(41)	53.78	(0.39)	2.41	(0.02)	4.04	(0.50)
	$1 \cdot 10^{-2}$	2919	(50)	59.25	(0.42)	2.63	(0.06)	4.51	(0.36)
	$9 \cdot 10^{-2}$	2898	(29)	65.91	(0.55)	2.90	(0.05)	3.66	(0.29)
PLAo90	$1 \cdot 10^{-5}$	2824	(25)	45.67	(0.39)	2.18	(0.05)	2.85	(0.34)
	$1 \cdot 10^{-4}$	2911	(23)	50.15	(0.80)	2.28	(0.01)	3.22	(0.23)
	$1 \cdot 10^{-3}$	2995	(18)	56.29	(0.48)	2.39	(0.02)	3.10	(0.36)
	$1 \cdot 10^{-2}$	2990	(36)	60.17	(0.92)	2.55	(0.01)	3.68	(0.09)
	$9 \cdot 10^{-2}$	2948	(30)	65.91	(0.71)	2.81	(0.04)	3.17	(0.34)
PLAoISO	$1 \cdot 10^{-5}$	2934	(43)	48.12	(0.52)	2.34	(0.03)	2.92	(0.27)
	$1 \cdot 10^{-4}$	2924	(29)	51.94	(0.37)	2.31	(0.01)	3.58	(0.40)
	$1 \cdot 10^{-3}$	2975	(42)	56.01	(0.49)	2.42	(0.03)	4.02	(0.28)
	$1 \cdot 10^{-2}$	2996	(14)	61.12	(0.74)	2.61	(0.03)	3.14	(0.28)
	$9 \cdot 10^{-2}$	2903	(28)	67.27	(0.66)	2.88	(0.03)	3.52	(0.44)

Appendix

See Tables A.1 and A.2.

References

[1] ISO/ASTM 52900, Additive Manufacturing - General Principles - Terminology, 2015.

[2] B. Turner, R. Strong, S. Gold, A review of melt extrusion additive manufacturing processes: I. Process design and modeling, Rapid Prototyp. J. 20 (3) (2014) 192–204, http://dx.doi.org/10.1108/RPJ-01-2013-0012.

[3] J. Dizon, A. Espera Jr., Q. Chen, R. Advincula, Mechanical characterization of 3D-printed polymers, Addit. Manuf. 20 (2018) 44–67, http://dx.doi.org/10.1016/j.addma.2017.12.002.

[4] J. Chacón, M. Caminero, E. García-Plaza, P. Núñez, Additive manufacturing of PLA structures using fused deposition modelling: Effect of process parameters on mechanical properties and their optimal selection, Mater. Des. 124 (2017) 143–157, http://dx.doi.org/10.1016/j.matdes.2017.03.065.

[5] Y. Song, Y. Li, W. Song, K. Yee, K.-Y. Lee, V. Tagarielli, Measurements of the mechanical response of unidirectional 3D-printed PLA, Mater. Des. 123 (2017) 154–164, http://dx.doi.org/10.1016/j.matdes.2017.03.051.

[6] F. Arbeiter, M. Spoerk, J. Wiener, A. Gosch, G. Pinter, Fracture mechanical characterization and lifetime estimation of near-homogeneous components produced by fused filament fabrication, Polym. Test. 66 (2018) 105–113, http://dx.doi.org/10.1016/j.polymertesting.2018.01.002.

[7] W. Verbeeten, M. Lorenzo-Bañuelos, P. Arribas-Subiñas, Anisotropic rate-dependent mechanical behavior of poly(lactic acid) processed by material extrusion additive manufacturing, Addit. Manuf. 31 (2020) 100968, http://dx.doi.org/10.1016/j.addma.2019.100968.

[8] Q. Sun, G. Rizvi, C. Bellehumeur, P. Gu, Effect of processing conditions on the bonding quality of FDM polymer filaments, Rapid Prototyp. J. 14 (2) (2008) 72–80, http://dx.doi.org/10.1108/13552540810862028.

[9] C. Kousiatza, D. Karalekas, In-situ monitoring of strain and temperature distributions during fused deposition modeling process, Mater. Des. 97 (2016) 400–406, http://dx.doi.org/10.1016/j.matdes.2016.02.099.

[10] J. Seppala, K. Migler, Infrared thermography of welding zones produced by polymer extrusion additive manufacturing, Addit. Manuf. 12 (2016) 71–76, http://dx.doi.org/10.1016/j.addma.2016.06.007.

[11] M. Mackay, The importance of rheological behavior in the additive manufacturing technique material extrusion, J. Rheol. 62 (6) (2018) 1549–1561, http://dx.doi.org/10.1122/1.5037687.

[12] V. Srinivas, C. van Hooy-Corstjens, J. Harings, Correlating molecular and crystallization dynamics to macroscopic fusion and thermodynamic stability in fused deposition modeling; a model study on polylactides, Polymer 142 (2018) 348–355, http://dx.doi.org/10.1016/j.polymer.2018.03.063.

[13] C. McIlroy, R. Graham, Modelling flow-enhanced crystallisation during fused filament fabrication of semi-crystalline polymer melts, Addit. Manuf. 24 (2018) 323–340, http://dx.doi.org/10.1016/j.addma.2018.10.018.

[14] L. Northcutt, S. Orski, K. Migler, A. Kotula, Effect of processing conditions on crystallization kinetics during materials extrusion additive manufacturing, Polymer 154 (2018) 182–187, http://dx.doi.org/10.1016/j.polymer.2018.09.018.

[15] A. Abbott, G. Tandon, R. Bradford, H. Koerner, J. Baur, Process-structure–property effects on ABS bond strength in fused filament fabrication, Addit. Manuf. 19 (2018) 29–38, http://dx.doi.org/10.1016/j.addma.2017.11.002.

[16] J. Rodríguez, J. Thomas, J. Renaud, Mechanical behavior of acrylonitrile butadiene styrene (ABS) fused deposition materials. Experimental investigation, Rapid Prototyp. J. 7 (3) (2001) 148–158, http://dx.doi.org/10.1108/13552540110395547.

[17] C. McIlroy, P. Olmsted, Disentanglement effects on welding behaviour of polymer melts during the fused-filament-fabrication method for additive manufacturing, Polymer 123 (2017) 376–391, http://dx.doi.org/10.1016/j.polymer.2017.06.051.

[18] W. Verbeeten, R. Arnold-Bik, M. Lorenzo-Bañuelos, Print velocity effects on strain-rate sensitivity of acrylonitrile-butadiene-styrene using material extrusion additive manufacturing, Polymers 13 (1) (2021) 149, http://dx.doi.org/10.3390/polym13010149.

[19] D. Vaes, P. Van Puyvelde, Semi-crystalline feedstock for filament-based 3D printing of polymers, Prog. Polym. Sci. 118 (2021) 101411, http://dx.doi.org/10.1016/j.progpolymsci.2021.101411.

[20] L. Li, Q. Sun, C. Bellehumeur, P. Gu, Composite modeling and analysis for fabrication of FDM prototypes with locally controlled properties, J. Manuf. Proc. 4 (2) (2002) 129–141, http://dx.doi.org/10.1016/S1526-6125(02)70139-4.

[21] J. Rodríguez, J. Thomas, J. Renaud, Design of fused-deposition ABS components for stiffness and strength, J. Mech. Des. 125 (3) (2003) 545–551, http://dx.doi.org/10.1115/1.1582499.

[22] A. Lanzotti, M. Grasso, G. Staiano, M. Martorelli, The impact of process parameters on mechanical properties of parts fabricated in PLA with an open-source 3-D printer, Rapid Prototyp. J. 21 (5) (2015) 604–617, http://dx.doi.org/10.1108/RPJ-09-2014-0135.

[23] M. Dawoud, I. Taha, S. Ebeid, Mechanical behaviour of ABS: An experimental study using FDM and injection moulding techniques, J. Manuf. Proc. 21 (2016) 39–45, http://dx.doi.org/10.1016/j.jmapro.2015.11.002.

[24] A. Ahmed, L. Susmel, Additively manufactured PLA under static loading: strength/cracking behaviour vs. deposition angle, Proc. Struct. Int. 3 (2017) 498–507, http://dx.doi.org/10.1016/j.prostr.2017.04.060.

[25] S. Kain, J. Ecker, A. Haider, M. Musso, A. Petutschnigg, Effects of the infill pattern on mechanical properties of fused layer modeling (FLM) 3D printed wood/polylactic acid (PLA) composites, Eur. J. Wood Wood Prod. 78 (1) (2020) 65–74, http://dx.doi.org/10.1007/s00107-019-01473-0.

[26] V. Azzi, S. Tsai, Anisotropic strength of composites, Exp. Mech. 5 (9) (1965) 283–288, http://dx.doi.org/10.1007/BF02326292.

[27] M. Afrose, S. Masood, P. Iovenitti, M. Nikzad, I. Sbarski, Effects of part build orientations on fatigue behaviour of FDM-processed PLA material, Prog. Addit. Manuf. 1 (1–2) (2016) 21–28, http://dx.doi.org/10.1007/s40964-015-0002-3.

[28] G.H. Staab, 6 - laminate analysis, in: Laminar Composites, second ed., Butterworth-Heinemann, 2015, pp. 189–284, http://dx.doi.org/10.1016/B978-0-12-802400-3.00006-4.

[29] B. Tymrak, M. Kreiger, J. Pearce, Mechanical properties of components fabricated with open-source 3-D printers under realistic environmental conditions, Mater. Des. 58 (2014) 242–246, http://dx.doi.org/10.1016/j.matdes.2014.02.038.

[30] F. Ning, W. Cong, Y. Hu, H. Wang, Additive manufacturing of carbon fiber-reinforced plastic composites using fused deposition modeling: Effects of process parameters on tensile properties, J. Compos. Mater. 51 (4) (2017) 451–462, http://dx.doi.org/10.1177/0021998316646169.

[31] E. Papon, A. Haque, Fracture toughness of additively manufactured carbon fiber reinforced composites, Addit. Manuf. 26 (2019) 41–52, http://dx.doi.org/10.1016/j.addma.2018.12.010.

[32] S.-H. Ahn, M. Montero, D. Odell, S. Roundy, P. Wright, Anisotropic material properties of fused deposition modeling ABS, Rapid Prototyp. J. 8 (4) (2002) 248–257, http://dx.doi.org/10.1108/13552540210441166.

[33] B. Kaplun, R. Zhou, K. Jones, M. Dunn, C. Yakacki, Influence of orientation on mechanical properties for high-performance fused filament fabricated ultem 9085 and electro-statically dissipative polyetherketoneketone, Addit. Manuf. 36 (2020) 101527, http://dx.doi.org/10.1016/j.addma.2020.101527.

[34] S. Messimer, T. Rocha Pereira, A. Patterson, M. Lubna, F. Drozda, Full-density fused deposition modeling dimensional error as a function of raster angle and build orientation: Large dataset for eleven materials, J. Manuf. Mater. Proc. 3 (1) (2019) 6, http://dx.doi.org/10.3390/jmmp3010006.

[35] C. Bert, T. Chen, Effect of shear deformation on vibration of antisymmetric angle-ply laminated rectangular plates, Int. J. Solids Struct. 14 (6) (1978) 465–473, http://dx.doi.org/10.1016/0020-7683(78)90011-2.

[36] M.M. Bertoldi, P.C.M. Yardimci, S. Güceri, G. Sala, Mechanical characterization of parts processed via fused deposition, Solid Freeform Fabr. Symp. 9 (1998) 557–565.

[37] T. Ree, H. Eyring, Theory of non-Newtonian flow. I. Solid plastic system, J. Appl. Phys. 26 (7) (1955) 793–800, http://dx.doi.org/10.1063/1.1722098.

[38] R. Haward, G. Thackray, The use of a mathematical model to describe isothermal stress-strain curves in glassy thermoplastics, Proc. R. Soc. A 302 (1471) (1968) 453–472, http://dx.doi.org/10.1098/rspa.1968.0029.

[39] C. Bauwens-Crowet, J. Bauwens, G. Homès, Tensile yield-stress behavior of glassy polymers, J. Polym. Sci. A-2: Polym. Phys. 7 (4) (1969) 735–742, http://dx.doi.org/10.1002/pol.1969.160070411.

[40] E. Klompen, L. Govaert, Nonlinear viscoelastic behaviour of thermorheologically complex materials, Mech. Time-Dep. Mater. 3 (1) (1999) 49–69, http://dx.doi.org/10.1023/A:1009853024441.

[41] R. Janssen, D. de Kanter, L. Govaert, H. Meijer, Fatigue life predictions for glassy polymers: A constitutive approach, Macromolecules 41 (7) (2008) 2520–2530, http://dx.doi.org/10.1021/ma071273i.

[42] T. Engels, S. Söntjens, T. Smit, L. Govaert, Time-dependent failure of amorphous polylactides in static loading conditions, J. Mater. Sci.-Mater. Med. 21 (1) (2010) 89–97, http://dx.doi.org/10.1007/s10856-009-3851-9.

[43] M. Kanters, K. Remerie, L. Govaert, A new protocol for accelerated screening of long-term plasticity-controlled failure of polyethylene pipe grades, Polym. Eng. Sci. 56 (6) (2016) 676–688, http://dx.doi.org/10.1002/pen.24294.

[44] H. Eyring, Viscosity, plasticity, and diffusion as examples of absolute reaction rates, J. Chem. Phys. 4 (4) (1936) 283–291, http://dx.doi.org/10.1063/1.1749836.

[45] W. Verbeeten, M. Sánchez-Soto, M. Maspoch, Hydrostatic pressure dependence in tensile and compressive behavior of an acrylonitrile-butadiene-styrene (ABS) copolymer, J. Appl. Polym. Sci. 139 (23) (2022) e52295, http://dx.doi.org/10.1002/app.52295.

[46] L. van Breemen, T. Engels, E. Klompen, D. Senden, L. Govaert, Rate- and temperature-dependent strain softening in solid polymers, J. Polym. Sci. B: Polym. Phys. 50 (24) (2012) 1757–1771, http://dx.doi.org/10.1002/polb.23199.

[47] C. Bauwens-Crowet, The compression yield behaviour of polymethyl methacrylate over a wide range of temperatures and strain-rates, J. Mater. Sci. 8 (7) (1973) 968–979, http://dx.doi.org/10.1007/BF00756628.

[48] M. Boyce, D. Parks, A. Argon, Large inelastic deformation of glassy polymers. part I: rate dependent constitutive model, Mech. Mater. 7 (1) (1988) 15–33, http://dx.doi.org/10.1016/0167-6636(88)90003-8.

[49] P. Wu, E. van der Giessen, On improved network models for rubber elasticity and their applications to orientation hardening in glassy polymers, J. Mech. Phys. Solids 41 (3) (1993) 427–456, http://dx.doi.org/10.1016/0022-5096(93)90043-F.

[50] C. Buckley, D. Jones, Glass-rubber constitutive model for amorphous polymers near the glass transition, Polymer 36 (17) (1995) 3301–3312, http://dx.doi.org/10.1016/0032-3861(95)99429-X.

[51] E. Klompen, T. Engels, L. Govaert, H. Meijer, Modeling of the postyield response of glassy polymers: Influence of thermomechanical history, Macromolecules 38 (16) (2005) 6997–7008, http://dx.doi.org/10.1021/ma050498v.

[52] Z. Tadmor, Molecular orientation in injection molding, J. Appl. Polym. Sci. 18 (6) (1974) 1753–1772, http://dx.doi.org/10.1002/app.1974.070180614.

[53] T. van Erp, L. Govaert, G. Peters, Mechanical performance of injection-molded poly(propylene): Characterization and modeling, Macromol. Mater. Eng. 298 (3) (2013) 348–358, http://dx.doi.org/10.1002/mame.201200116.

[54] D. Senden, G. Peters, L. Govaert, J. van Dommelen, Anisotropic yielding of injection molded polyethylene: Experiments and modeling, Polymer 54 (21) (2013) 5899–5908, http://dx.doi.org/10.1016/j.polymer.2013.08.047.

[55] J. Roetling, Yield stress behaviour of polymethylmethacrylate, Polymer 6 (6) (1965) 311–317, http://dx.doi.org/10.1016/0032-3861(65)90081-9.

[56] L. Govaert, P. Timmermans, W. Brekelmans, The influence of intrinsic strain softening on strain localization in polycarbonate: Modeling and experimental validation, J. Eng. Mater. Technol. 122 (2) (2000) 177–185, http://dx.doi.org/10.1115/1.482784.

[57] J. Sauer, D. Mears, K. Pae, Effects of hydrostatic pressure on the mechanical behaviour of polytetrafluoroethylene and polycarbonate, Eur. Polym. J. 6 (7) (1970) 1015–1022, http://dx.doi.org/10.1016/0014-3057(70)90034-0.

[58] I. Ward, Review: The yield behaviour of polymers, J. Mater. Sci. 6 (11) (1971) 1397–1417, http://dx.doi.org/10.1007/BF00549685.

[59] C. Bauwens-Crowet, J.-C. Bauwens, G. Homès, The temperature dependence of yield of polycarbonate in uniaxial compression and tensile tests, J. Mater. Sci. 7 (2) (1972) 176–183, http://dx.doi.org/10.1007/BF00554178.

[60] L. Govaert, H. Schellens, H. Thomassen, R. Smit, L. Terzoli, T. Peijs, A micromechanical approach to time-dependent failure in off-axis loaded polymer composites, Composites A 32 (12) (2001) 1697–1711, http://dx.doi.org/10.1016/S1359-835X(01)00028-8.

[61] E. Arruda, M. Boyce, R. Jayachandran, Effects of strain rate, temperature and thermomechanical coupling on the finite strain deformation of glassy polymers, Mech. Mater. 19 (2–3) (1995) 193–212, http://dx.doi.org/10.1016/0167-6636(94)00034-E.

[62] H. Starkweather, P. Avakian, J. Fontanella, M. Wintersgill, Internal motions in polylactide and related polymers, Macromolecules 26 (19) (1993) 5084–5087, http://dx.doi.org/10.1021/ma00071a016.

[63] J. Ren, O. Urakawa, K. Adachi, Dielectric and viscoelastic studies of segmental and normal mode relaxations in undiluted poly(d, l-lactic acid), Macromolecules 36 (1) (2003) 210–219, http://dx.doi.org/10.1021/ma0212341.

[64] J. Badia, L. Monreal, V. Sáenz de Juano-Arbona, A. Ribes-Greus, Dielectric spectroscopy of recycled polylactide, Polym. Degrad. Stab. 107 (2014) 21–27, http://dx.doi.org/10.1016/j.polymdegradstab.2014.04.023.

[65] D. Grijpma, A. Pennings, (Co)polymers of L-lactide, 2. Mechanical properties, Macromol. Chem. Phys. 195 (5) (1994) 1649–1663, http://dx.doi.org/10.1002/macp.1994.021950516.

[66] S. Park, M. Todo, K. Arakawa, M. Koganemaru, Effect of crystallinity and loading-rate on mode I fracture behavior of poly(lactic acid), Polymer 47 (4) (2006) 1357–1363, http://dx.doi.org/10.1016/j.polymer.2005.12.046.

[67] C. McIlroy, P. Olmsted, Deformation of an amorphous polymer during the fused-filament-fabrication method for additive manufacturing, J. Rheol. 61 (2) (2017) 379–397, http://dx.doi.org/10.1122/1.4976839.

[68] A. Costanzo, R. Spotorno, M. Candal, M. Fernández, A. Müller, R. Graham, D. Cavallo, C. McIlroy, Residual alignment and its effect on weld strength in material-extrusion 3D-printing of polylactic acid, Addit. Manuf. 36 (2020) 101415, http://dx.doi.org/10.1016/j.addma.2020.101415.

[69] P. Coates, I. Ward, The plastic deformation behaviour of linear polyethylene and polyoxymethylene, J. Mater. Sci. 13 (9) (1978) 1957–1970, http://dx.doi.org/10.1007/BF00552903.

[70] P. Botto, R. Duckett, I. Ward, The yield and thermoelastic properties of oriented poly(methyl methacrylate), Polymer 28 (2) (1987) 257–262, http://dx.doi.org/10.1016/0032-3861(87)90414-9.

[71] P. Hope, I. Ward, An activated rate theory approach to the hydrostatic extrusion of polymers, J. Mater. Sci. 16 (6) (1981) 1511–1521, http://dx.doi.org/10.1007/BF02369868.

[72] D. Senden, J. van Dommelen, L. Govaert, Strain hardening and its relation to Bauschinger effects in oriented polymers, J. Polym. Sci. B: Polym. Phys. 48 (13) (2010) 1483–1494, http://dx.doi.org/10.1002/polb.22056.

[73] L. Jiang, J. Zhang, M. Wolcott, Comparison of polylactide/nano-sized calcium carbonate and polylactide/montmorillonite composites: Reinforcing effects and toughening mechanisms, Polymer 48 (26) (2007) 7632–7644, http://dx.doi.org/10.1016/j.polymer.2007.11.001.

[74] B. Wittbrodt, J. Pearce, The effects of PLA color on material properties of 3-D printed components, Addit. Manuf. 8 (2015) 110–116, http://dx.doi.org/10.1016/j.addma.2015.09.006.

[75] J. Bustillos, D. Montero, P. Nautiyal, A. Loganathan, B. Boesl, A. Agarwal, Integration of graphene in poly(lactic) acid by 3D printing to develop creep and wear-resistant hierarchical nanocomposites, Polym. Compos. 39 (11) (2018) 3877–3888, http://dx.doi.org/10.1002/pc.24422.